

Fixed-target charmonium production and pion parton distributions

Wen-Chen Chang,¹ Jen-Chieh Peng,² Stephane Platchkov,³ and Takahiro Sawada⁴

¹*Institute of Physics, Academia Sinica, Taipei 11529, Taiwan*

²*Department of Physics, University of Illinois at Urbana-Champaign, Urbana, Illinois 61801, USA*

³*IRFU, CEA, Université Paris-Saclay, 91191 Gif-sur-Yvette, France*

⁴*Nambu Yoichiro Institute of Theoretical and Experimental Physics,
Osaka Metropolitan University, Osaka 558-8585, Japan*

(Dated: March 9, 2023)

We investigate how charmonium hadroproduction at fixed-target energies can be used to constrain the gluon distribution in pions. Using nonrelativistic QCD (NRQCD) formulation, the J/ψ and $\psi(2S)$ cross sections as a function of longitudinal momentum fraction x_F from pions and protons colliding with light targets, as well as the $\psi(2S)$ to J/ψ cross section ratios, are included in the analysis. The color-octet long-distance matrix elements are found to have a pronounced dependence on the pion parton distribution functions (PDFs). This study shows that the x_F differential cross sections of pion-induced charmonium production impose strong constraints on the pion's quark and gluon PDFs. In particular, the pion PDFs with larger gluon densities provide a significantly better description of the data. It is also found that the production of the $\psi(2S)$ state is associated with a larger quark-antiquark contribution, compared with J/ψ .

I. INTRODUCTION

The pion, as the lightest QCD bound state, plays an essential role in the nucleon-nucleon interactions over nuclear-size distances [1]. Theoretically, its partonic structure is easier to construct than that of the nucleon. Pion distribution amplitudes and parton distribution functions (PDFs) have been predicted by a number of recent calculations based on the chiral-quark model [2–4], Nambu-Jona-Lasinio model [5], light-front Hamiltonian [6–8], holographic QCD [9–11], maximum entropy method [12, 13], Dyson-Schwinger equations (DSE) [14–24], and lattice QCD [25–37]. In contrast, the partonic structure of pion is much less explored experimentally, due to the absence of a pion target. The present knowledge on the pion PDFs comes primarily from fixed-target pion-induced Drell-Yan (DY) measurements [38]. However, the DY data are mainly sensitive to the valence-quark distributions, leaving the sea and gluon distributions essentially unknown. The sea-quark contributions can in principle be extracted by comparing measurements with the positive and negative pion beams [39], although the existing measurements are scarce and of insufficient statistical accuracy.

The gluon distribution in the pion can be accessed through processes such as prompt-photon production [40], leading-neutron deep-inelastic scattering (DIS) [41, 42] or heavy quarkonia production [43, 44]. Each of these processes has its own advantages and limitations. With the exception of Ref. [45], the pion-induced J/ψ and $\psi(2S)$ production data were not included in the global analysis, possibly reflecting the concern that the production mechanism for charmonium production was not well understood. Significant progress in understanding the J/ψ production mechanism has been made in recent decades, and it is timely to investigate how the charmonium production data can provide useful constraints on the pion PDFs.

The theoretical challenge in describing the charmonium production comes from the treatment of the hadronization of $c\bar{c}$ pairs into a charmonium bound state [46, 47]. This nonperturbative process has been modeled in several theoretical ap-

proaches including the color evaporation model (CEM) [48–50], the color-singlet model (CSM) [51–53], and nonrelativistic QCD (NRQCD) [54]. The CEM, although successful for some observables, fails to explain some others observables in charmonium production [55]. Within the more rigorous NRQCD framework, the production of the heavy quark pair is treated perturbatively, whereas its hadronization to a bound state is described in terms of a set of long-distance matrix elements (LDMEs), extracted phenomenologically from the data.

From the experimental perspective, charmonium production has one important advantage: the cross sections are large, between one to two orders of magnitude higher than the DY ones, depending on the experimental conditions. A large number of fixed-target charmonium production experiments have been performed in the past, including experiments with pion beams [56, 57]. These data, collected mostly at CERN or at Fermilab, provide a wealth of additional information on the pion structure, and are expected to shed new light on its gluon distribution.

In this paper we investigate how charmonium production could help to differentiate between the available pion PDFs by imposing further constraints on the gluon distribution function [58, 59]. In the fixed-target energy domain, charmonium production is dominated by the quark-antiquark annihilation ($q\bar{q}$) and gluon-gluon fusion (GG) partonic subprocesses. The longitudinal momentum x_F -differential cross sections are sensitive to the quark and gluon parton distributions of the colliding hadrons. Since the nucleon PDFs are known with good accuracy, these differential cross sections should provide additional constraints on the pion's quark and gluon PDFs.

To perform this study, we employ the NRQCD framework, along the lines developed in Ref. [60]. Although limited to leading order (LO), this approach provides an adequate description of the fixed-target J/ψ and $\psi(2S)$ production data and can be used as a tool for accessing the pion PDFs. Our primary goal is to obtain a good phenomenological description of both pion and proton-induced data, and to explore the sensitivity of the results to the pion quark-gluon structure. As-

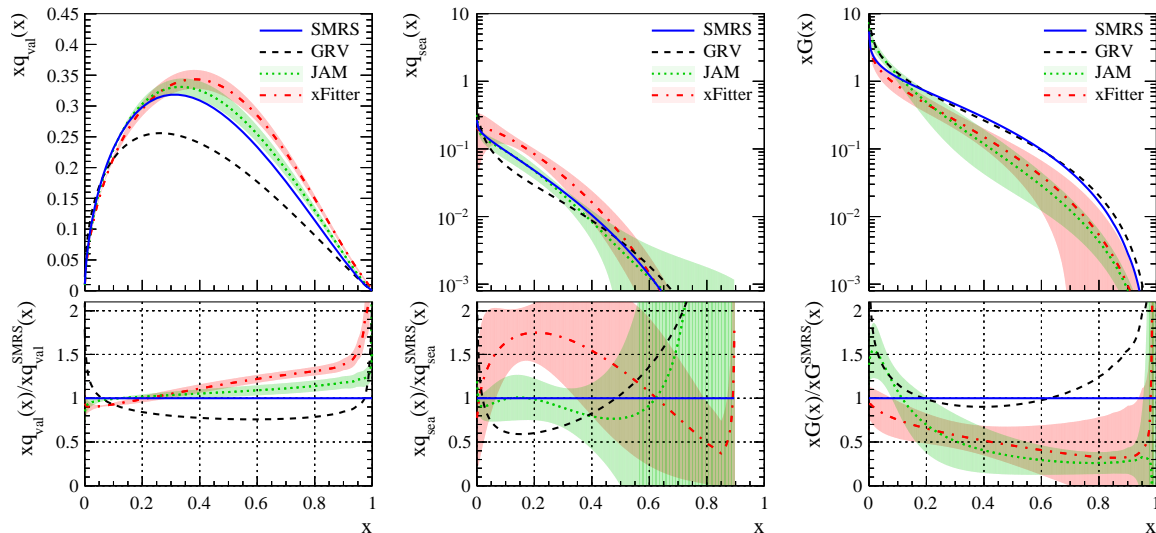


FIG. 1. Momentum density distributions $[xf(x)]$ of valence quarks, sea quarks and gluons of SMRS, GRV, xFitter and JAM pion PDFs and their ratios to the SMRS PDFs, at the scale of J/ψ mass ($Q^2 = 9.6 \text{ GeV}^2$). The uncertainty bands associated with JAM and xFitter PDFs are also shown.

suming that the LDMEs are independent of the beam species, the proton-induced cross sections are also included in this analysis. Since the proton PDFs are well known, the proton-induced data should help constraining the values of LDMEs common to both the proton and pion data.

Results of an earlier study limited to total cross sections of charmonium production were recently reported [59]. A new set of color-octet LDMEs, leading to a good agreement between the charmonium production data and the NRQCD fit was obtained. Here, we extend the study by including the x_F -dependent cross sections for J/ψ and $\psi(2S)$ production as well as their ratios for both pion and proton beams in the global fit. The distributions of the differential x_F cross sections are calculated by convolving the partonic cross sections, the LDMEs of the various subprocesses and the associated beam and target parton densities. An adequate NRQCD description of such a large dataset should impose a strong constrain on the pion PDFs. In order to minimize nuclear matter effects that are not well understood, the present analysis is limited to data taken with the lightest targets available: hydrogen, lithium and beryllium. Data with heavier targets were considered only for the J/ψ to $\psi(2S)$ cross section ratios, assuming nuclear effects are largely independent of the charmonium states.

This paper is organized as follows. In Sec. II, we describes distinctive features of parton densities in four pion PDFs. The NRQCD formalism used for this study is introduced in Sec. III. Section IV briefly describes the J/ψ and $\psi(2S)$ datasets used in the global fit. We present the results of NRQCD calculations using various pion PDFs and the comparison with the charmonium data in Sec. V. Finally we comment on the fit results in Sec. VI and conclude in Sec. VII

II. PION PDFS

As mentioned before, pion-induced Drell-Yan data are used in all global analyses for constraining the valence-quark distribution of the pion PDFs. Without data from other processes, the sea and gluon distributions can only be inferred through the momentum sum rule and valence-quark sum rule. The two most recent global analyses dedicated to the extraction of the pion PDFs are JAM [61–63] and xFitter [64]. The two groups consider the same DY data, but differ in the choice of the pion-induced processes. The xFitter group makes use of the pion-induced prompt-photon production data, whereas the JAM collaboration includes the leading-neutron DIS cross section measurements instead. The Sutton-Martin-Roberts-Stirling (SMRS) global fit [65] also incorporates the prompt-photon data, but instead of calculating the fit uncertainties, it considers three different options for the gluon and sea contents. Another widely used parametrization is the fit of Gluck-Reya-Vogt (GRV) [66], in which the gluon and sea distributions are dynamically generated from the QCD evolution.

We utilize the LHAPDF framework [67, 68] to access these four pion PDFs for our study. The corresponding pion PDF sets are “SMRSPILHgrid”, “GRVPI1”, “JAM21PionPDFnlo”, and “xFitterPI_NLO_EIG”, respectively. Out of the three possible parametrizations for SMRS, we choose the one in which the sea quarks carry 15% of the pion momentum at $Q^2 = 4 \text{ GeV}^2$. Their valence, sea and gluon momentum distributions $xf(x)$ at the scale of J/ψ mass are compared in Fig. 1. Their ratios to SMRS are shown in the bottom panel. Within the range of $x \sim 0.1$ – 0.8 , the valence-quark distributions of SMRS, JAM and xFitter are close to each other, whereas GRV is lower by up to 20%–30%. Not surprisingly, the sea distribution is essentially unknown, as illustrated by the large variations between the four PDFs. The

gluon distributions also show sizable differences; e.g., in the region of $x > 0.2$ the xFitter and JAM distributions are smaller in comparison with SMRS and GRV, by up to a factor of 2-3.

III. HEAVY-QUARK PAIR PRODUCTION AND NRQCD MODEL

Within the NRQCD theoretical framework, the heavy quarkonium production is factorized into production of a heavy-quark pair ($Q\bar{Q}$) at the parton level, and its subsequent hadronization into quarkonium states. The $Q\bar{Q}$ production cross section can be calculated perturbatively [69–71], whereas the hadronization probability of the $Q\bar{Q}$ pair is encoded in the nonperturbative LDME parameters $\langle \mathcal{O}_n^H [^{2S+1}L_J] \rangle$, depending on the spin, orbital, and total angular momentum quantum numbers, S , L and J , respectively, and on the color configuration (n). Parity, charge conjugation and angular momentum conservation limit the allowed quantum numbers to only a few. The LDMEs are assumed to be universal, i.e., independent of the beam and target hadrons and of the energy scale. The color singlet (CS) LDMEs are typically determined from decay rate measurements using a potential model [72], while the color octet (CO) LDMEs are obtained from a fit to the experimental data.

In NRQCD, the differential cross section $d\sigma/dx_F$ for the production of a charmonium state H ($H = J/\psi, \psi(2S)$, or χ_{cJ}) from the hN collisions, where h is the beam hadron ($h = p, \bar{p},$ or π) and N the target nucleon, is expressed as [73]

$$\frac{d\sigma^H}{dx_F} = \sum_{i,j=q,\bar{q},G} \int_0^1 dx_1 dx_2 \delta(x_F - x_1 + x_2) \times f_i^h(x_1, \mu_F) f_j^N(x_2, \mu_F) \times \hat{\sigma}[ij \rightarrow H](x_1 P_h, x_2 P_N, \mu_F, \mu_R, m_c), \quad (1)$$

$$\hat{\sigma}[ij \rightarrow H] = \sum_n C_{c\bar{c}[n]}^{ij}(x_1 P_h, x_2 P_N, \mu_F, \mu_R, m_c) \times \langle \mathcal{O}_n^H [^{2S+1}L_J] \rangle \quad (2)$$

where the indexes i and j run over the type of interacting partons (gluons, quarks and antiquarks), and $C_{c\bar{c}[n]}^{ij}$ denotes the hard-QCD production cross section for $c\bar{c}$ pair. The parameter m_c is the charm quark mass; f^h and f^N are the incoming hadron and the target nucleon parton distribution functions, evaluated at their respective Bjorken- x values, x_1 and x_2 . The μ_F and μ_R are the factorization and renormalization scales. The Feynman variable x_F and the beam and target parton momentum fractions x_1 and x_2 are:

$$x_F = \frac{2p_L}{\sqrt{s}}, \quad x_{1,2} = \frac{(x_F^2 + 4M_{c\bar{c}}^2/s)^{1/2} \pm x_F}{2}. \quad (3)$$

Here $M_{c\bar{c}}$ and p_L are the mass and longitudinal momentum of the $c\bar{c}$ pair in the center-of-mass frame. The total cross sections are obtained by integrating over x_F .

In this study, we use the formula given in Ref. [60] for computation of $J/\psi, \psi(2S)$, and χ_{cJ} production via $GG, q\bar{q}$ and

qG subprocesses. The scattering subprocesses $q\bar{q} \rightarrow Q\bar{Q}$ and $GG \rightarrow Q\bar{Q}$ at $\mathcal{O}(\alpha_s^2)$ produce $Q\bar{Q}$ pairs in an S -wave CO state or P -wave CS state. Table I summarizes the relationships between the LDMEs and the scattering subprocesses for $J/\psi, \psi(2S), \chi_{c0}, \chi_{c1}$, and χ_{c2} , up to $\mathcal{O}(\alpha_s^3)$. For the $q\bar{q}$ subprocess, the $c\bar{c}$ pairs are produced at $\mathcal{O}(\alpha_s^2)$ in color octet states, which then hadronize into various charmonium states with the LDMEs $\langle \mathcal{O}_8^H [^3S_1] \rangle$. For the GG subprocess, both J/ψ , and $\psi(2S)$ can be produced from either the CO $c\bar{c}$ at $\mathcal{O}(\alpha_s^2)$ or the CS $c\bar{c}$ at $\mathcal{O}(\alpha_s^3)$. The CO $^1S_0, ^3P_0$, and 3P_2 are combined into a single LDME, Δ_8^H , via the relation: $\Delta_8^H = \langle \mathcal{O}_8^H [^1S_0] \rangle + \frac{3}{m_c^2} \langle \mathcal{O}_8^H [^3P_0] \rangle + \frac{4}{5m_c^2} \langle \mathcal{O}_8^H [^3P_2] \rangle$.

H	$q\bar{q}$	GG	qG
$J/\psi, \psi(2S)$	$\langle \mathcal{O}_8^H [^3S_1] \rangle (\alpha_s^2)$	$\Delta_8^H (\alpha_s^2)$ $\langle \mathcal{O}_1^H [^3S_1] \rangle (\alpha_s^3)$	
χ_{c0}	$\langle \mathcal{O}_8^H [^3S_1] \rangle (\alpha_s^2)$	$\langle \mathcal{O}_1^H [^3P_0] \rangle (\alpha_s^3)$	
χ_{c1}	$\langle \mathcal{O}_8^H [^3S_1] \rangle (\alpha_s^2)$	$\langle \mathcal{O}_1^H [^3P_1] \rangle (\alpha_s^3)$	$\langle \mathcal{O}_1^H [^3P_1] \rangle (\alpha_s^3)$
χ_{c2}	$\langle \mathcal{O}_8^H [^3S_1] \rangle (\alpha_s^2)$	$\langle \mathcal{O}_1^H [^3P_2] \rangle (\alpha_s^3)$	

TABLE I. Relationship of LDMEs and the associated orders of α_s to the scattering subprocesses for various charmonium states in the NRQCD framework of Ref. [60]. Here $\Delta_8^H = \langle \mathcal{O}_8^H [^1S_0] \rangle + \frac{3}{m_c^2} \langle \mathcal{O}_8^H [^3P_0] \rangle + \frac{4}{5m_c^2} \langle \mathcal{O}_8^H [^3P_2] \rangle$.

The number of independent LDMEs is further reduced by applying the spin symmetry relations [60, 74]:

$$\begin{aligned} \langle \mathcal{O}_8^{J/\psi, \psi(2S)} [^3P_J] \rangle &= (2J+1) \langle \mathcal{O}_8^{J/\psi, \psi(2S)} [^3P_0] \rangle \text{ for } J=2 \\ \langle \mathcal{O}_8^{\chi_{cJ}} [^3S_1] \rangle &= (2J+1) \langle \mathcal{O}_8^{\chi_{c0}} [^3S_1] \rangle \text{ for } J=1, 2 \\ \langle \mathcal{O}_1^{\chi_{cJ}} [^3P_J] \rangle &= (2J+1) \langle \mathcal{O}_1^{\chi_{c0}} [^3P_0] \rangle \text{ for } J=1, 2. \end{aligned} \quad (4)$$

The LDMEs used in the present work exhibit sensitivity to different elementary scattering subprocesses contributing to the charmonium production. In the cases of J/ψ and $\psi(2S)$ production, the CO $\langle \mathcal{O}_8^H [^3S_1] \rangle$ LDME is related to the $q\bar{q} \rightarrow Q\bar{Q}$ subprocess, while the $GG \rightarrow Q\bar{Q}$ subprocess is strongly dependent on the Δ_8^H term. More details on the NRQCD framework used in this work can be found in Refs. [59, 60]. In the following study, the CS $\langle \mathcal{O}_1^H [^3S_1] \rangle$ LDMEs for J/ψ and $\psi(2S)$ and the CS $\langle \mathcal{O}_1^H [^3P_0] \rangle$ and CO $\langle \mathcal{O}_8^H [^3S_1] \rangle$ LDMEs for χ_{c0} are fixed to be 1.16, 0.76, 0.044 and 0.0032, respectively, which are the values used in Refs. [59, 60].

With the information of LDMEs, the direct production cross sections of $J/\psi, \psi(2S)$ and three χ_{cJ} states as a function of x_F can be evaluated as shown in Eq.(1). The J/ψ cross section is estimated taking into account the direct production of J/ψ and the feed-down from hadronic decays of $\psi(2S)$ and radiative decays of three χ_{cJ} states as follows,

$$\begin{aligned} \sigma_{J/\psi} &= \sigma_{J/\psi}^{direct} \\ &+ Br(\psi(2S) \rightarrow J/\psi X) \sigma_{\psi(2S)} \\ &+ \sum_{J=0}^2 Br(\chi_{cJ} \rightarrow J/\psi \gamma) \sigma_{\chi_{cJ}} \end{aligned} \quad (5)$$

The various branching ratios Br are taken from the PDG 2020 [75]: $Br(\psi(2S) \rightarrow J/\psi X) = 61.4\%$, $Br(\chi_{c0} \rightarrow J/\psi\gamma) = 1.4\%$, $Br(\chi_{c1} \rightarrow J/\psi\gamma) = 34.3\%$, and $Br(\chi_{c2} \rightarrow J/\psi\gamma) = 19.0\%$.

In the present analysis we use the convention of charm quark mass, factorization and renormalization scales in Ref. [60] for fixed-target hadroproduction of charmonium: $m_c = 1.5 \text{ GeV}/c^2$ and $\mu_F = \mu_R = 2m_c$. The uncertainties associated with this choice are evaluated by changing the reference scale from m_c to $3m_c$. The nucleon PDFs are taken from CTEQ14nlo [76]. For the lithium, beryllium, silicon, gold and tungsten targets, the nuclear EPPS16 PDFs [77] are used.

IV. OVERVIEW OF DATA USED

The present analysis is based on pion and proton-induced total and differential cross sections for J/ψ and $\psi(2S)$ production, and on the differential $R_\psi(x_F) = \sigma_{\psi(2S)}(x_F)/\sigma_{(J/\psi)}(x_F)$ ratios. The total cross sections for the pion-induced data were taken from the compilations made in Refs. [56] and [57]. The proton-induced total cross sections and ratios were taken from Ref. [74]. The proton-induced values for R_ψ from HERA-B [78] and NA38 [79] and the pion-induced ones from WA92 [80] and WA39 [81] were added to the selection. The x_F -differential cross sections for pion-induced J/ψ production [82–87] and $\psi(2S)$ production [82] were selected according to the targets used: hydrogen, lithium and beryllium. Datasets with heavier targets were not included. The same criterion was applied to the proton-induced J/ψ production [83, 84]. The $R_\psi(x_F)$ ratios were taken from Ref. [88] for the pion-induced production and from Refs. [78, 89–91] for the proton-induced one. Assuming that nuclear effects are identical for both charmonium states, no restriction on the target employed was applied.

The datasets with x_F dependent measurements are listed in Table II. In terms of pion-induced (proton-induced) data sets, there are 8 (2) for J/ψ production, 2 (0) for $\psi(2S)$ production and 1 (4) for $R_\psi(x_F)$. In total, there are 164 and 82 data points for the pion-induced and proton-induced data, respectively. The beam momenta of the datasets cover the range of 39.5–515 GeV/c, corresponding to \sqrt{s} values ranging from 8.6 to 31.1 GeV.

V. RESULTS OF NRQCD CALCULATIONS

A. Reference NRQCD calculations

Before performing a fit to the data listed in Table II to obtain the best-fit LDMEs for the four pion PDFs, we first carry out NRQCD calculations using the LDMEs found in a recent study [59], where only the pion and proton total cross section data were fitted. The values of the LDMEs, obtained separately for each pion PDF, are listed in Table III. We then compare the results of the NRQCD calculations for the x_F dependent charmonium production cross sections with the data

listed in Table II and shown in Fig. 2. We call these ‘‘Reference NRQCD calculation’’ (REF), which provides the reference information to be compared with that obtained later from a fit to the x_F -dependent cross section data. Note that Fig. 2 is for the SMRS pion PDFs, and similar figures for the other three pion PDFs can be found in the Supplemental Material [92].

The total χ^2/ndf , as well as the χ^2/ndp (ndp denotes ‘‘number of data points’’) for individual pion or proton datasets, are listed in Table III under the label ‘‘REF’’. Table III shows that the reduced χ^2/ndf for ‘‘REF’’ are quite large, suggesting that the LDMEs deduced from the fit to total cross section data are not optimal for describing the x_F -dependent data. A further investigation shows that a significant contribution to the overall χ^2 comes from the absolute normalization of the measured cross sections relative to the NRQCD calculations. Despite the poor agreement between the data and the calculation, it is interesting to note that calculations using the SMRS and GRV pion PDFs are in a better agreement with the data than the JAM and xFitter PDFs.

B. NRQCD fits

We now proceed to a refined determination of the color-octet $\langle \mathcal{O}_8^H [^3S_1] \rangle$ and Δ_8^H LDMEs for J/ψ and $\psi(2S)$ production by fitting the x_F differential cross sections and $R_\psi(x_F)$ ratios for proton and pion beams. To avoid double counting, total cross sections data that result from an integration over the associated differential cross sections are not included in the fit. We note that the NRQCD calculations do not require a normalization factor, as they predict absolute cross sections. However, the experimental x_F -dependent J/ψ and $\psi(2S)$ cross sections are associated with experimental normalization uncertainties δ_σ , as quoted in Table II. An attempt to fit the data without taking into account the normalization uncertainties only marginally reduces the total χ^2/ndf . In order to take into account these uncertainties, a normalization parameter F is added for each of the x_F -differential datasets. Accordingly, a penalty term of $((F - 1)/\delta_\sigma)^2$ is included in the calculation of the overall χ^2 . To avoid unrealistic values of F , we limit the deviation of F from 1.0 to be less than $2\delta_\sigma$. The results of this approach are labeled as ‘‘FIT’’ below.

Figure 2 shows the new fit to the data for x_F -differential data and ratios using the SMRS pion PDFs. The newly-determined LDMEs parameters are shown in Table III. Except for the J/ψ data of WA11, the new NRQCD fit provides a reasonably good description of data for both pion and proton beams. Table III shows that for all four pion PDFs and for nearly all datasets the individual χ^2/ndp are significantly improved. The displayed yellow uncertainty bands result from the scale and charm mass variations of charm quark mass m_c of 1.4 and 1.6 GeV/c² at $\mu_F = \mu_R = 2m_c$, and $\mu_F = \mu_R = 1$ and $4m_c$ at $m_c = 1.5 \text{ GeV}/c^2$. The uncertainty is evaluated by the square root of the sum of squares of the cross section difference due to the individual variation. The corresponding LDMEs are obtained from a new global fit for each configuration. The uncertainty bands are relatively small and do not

Experiment	Beam	P_{beam} (GeV/c)	Target	Data	x_F	ndf	Norma. ^a	Ref.
FNAL E672, E706	π	515	Be	$\sigma^{J/\psi}$	[0.11, 0.79]	35	12.0	[82]
FNAL E705	π	300	Li	$\sigma^{J/\psi}$	[-0.10, 0.45]	12	9.5	[83]
CERN NA3 ^b	π	280	p	$\sigma^{J/\psi}$	[0.025, 0.825]	17	13.0	[84]
CERN NA3 ^b	π	200	p	$\sigma^{J/\psi}$	[0.05, 0.75]	8	13.0	[84]
CERN WA11 ^b	π	190	Be	$\sigma^{J/\psi}$	[-0.35, 0.75]	12	^c 10.0	[85]
CERN NA3 ^b	π	150	p	$\sigma^{J/\psi}$	[0.025, 0.925]	19	13.0	[84]
FNAL E537	π	125	Be	$\sigma^{J/\psi}$	[0.05, 0.95]	10	6.0	[86]
CERN WA39 ^b	π	39.5	p	$\sigma^{J/\psi}$	[0.05, 0.85]	9	15.0	[87]
FNAL E672, E706	π	515	Be	$\sigma^{\psi(2S)}$	[0.17, 0.73]	5	16.0	[82]
FNAL E615	π	253	W	$\sigma^{\psi(2S)}/\sigma^{J/\psi}$	[0.275, 0.975]	15		[88]
HERA-B	p	920	W	$\sigma^{\psi(2S)}/\sigma^{J/\psi}$	[-0.3, 0.075]	8		[78]
CERN NA50	p	450	W	$\sigma^{\psi(2S)}/\sigma^{J/\psi}$	[-0.075, 0.075]	4		[89]
FNAL E789	p	800	Au	$\sigma^{\psi(2S)}/\sigma^{J/\psi}$	[0.00, 0.12]	5		[90]
FNAL E771	p	800	Si	$\sigma^{\psi(2S)}/\sigma^{J/\psi}$	[0.00, 0.20]	6		[91]
FNAL E705	p	300	Li	$\sigma^{J/\psi}$	[-0.10, 0.45]	12	10.1	[83]
CERN NA3 ^b	p	200	p	$\sigma^{J/\psi}$	[0.05, 0.75]	8	13.0	[84]

TABLE II. Differential cross sections datasets for charmonium production [J/ψ , $\psi(2S)$ and $R_\psi(x_F)$] used in the study, listed in order of decreasing beam momentum.

^aPercentage of uncertainty in the cross section normalization.

^bThe numerical information was extracted from the published figures.

^cInformation not available but an educated guess .

	SMRS		GRV		JAM		xFitter	
	REF	FIT	REF	FIT	REF	FIT	REF	FIT
χ^2_{total}/ndf	5.7	1.9	7.0	2.4	17.7	5.6	14.3	4.2
$\chi^2/ndp _{x_F}^{\pi^-}$	5.3	1.8	7.6	2.4	25.5	5.9	19.5	4.5
$\chi^2/ndp _{x_F}^p$	10.7	1.6	10.5	1.7	11.2	2.7	11.5	1.9
$\chi^2/ndp _{\sqrt{s}}^{\pi^-}$	2.1	8.7	2.9	5.6	5.3	11.4	4.8	4.4
$\chi^2/ndp _{\sqrt{s}}^p$	3.8	8.1	3.4	8.1	3.5	5.1	3.6	6.9
$\langle \mathcal{O}_8^{J/\psi} [^3S_1] \rangle$	0.0690	0.0259±0.0023	0.0950	0.0432±0.0038	0.0830	0.1192±0.0021	0.0740	0.0849±0.0041
$\Delta_8^{J/\psi}$	0.0250	0.0560±0.0016	0.0180	0.0521±0.0017	0.0200	0.0244±0.0016	0.0220	0.0393±0.0034
$\langle \mathcal{O}_8^{\psi(2S)} [^3S_1] \rangle$	0.0210	0.0132±0.0009	0.0260	0.0210±0.0013	0.0260	0.0237±0.0009	0.0230	0.0186±0.0012
$\Delta_8^{\psi(2S)}$	0.0017	0.0057±0.0003	0.0004	0.0042±0.0003	0.0004	0.0021±0.0003	0.0009	0.0040±0.0006

TABLE III. Results of the NRQCD calculation using the reference values of the LDMEs (columns labeled “REF”) and of the fit of the LDMEs to the differential cross sections (columns “FIT”). The upper part of the table gives the values of the reduced χ^2/ndf of the entire dataset and the χ^2 divided by the number of data point (ndp) for the pion-induced and proton-induced datasets separately. The subscript x_F or \sqrt{s} for χ^2/ndp refers to x_F -dependent data or \sqrt{s} -dependent x_F -integrated data. The lower part of the table displays the values of the reference and fitted LDMEs for SMRS, GRV, JAM and xFitter pion PDFs. All LDMEs are in units of GeV^3 .

introduce an essential change in the quality of data description. The systematic studies are further discussed in Sec. V F. Similar figures for GRV, JAM and xFitter are available in the Supplemental Material [92].

Table III also lists the χ^2 values for both the “REF” and “FIT” calculations. The χ^2/ndp and the fitted normalization factors for each dataset are summarized in Table IV. The improved description of the differential cross sections is also confirmed by the overall χ^2_{total}/ndf and the χ^2/ndp values for various datasets. The χ^2/ndp of the pion-induced x_F datasets, $\chi^2/ndp|_{x_F}^{\pi^-}$, are 1.8, 2.4, 5.9 and 4.5 for the SMRS, GRV, JAM and xFitter PDFs, respectively, an improvement of about

a factor of three over that of “REF”. As expected, the χ^2/ndp of the proton-induced x_F datasets, $\chi^2/ndp|_{x_F}^p$, are of similar values, around 2.0 for all four pion PDFs. In contrast, the χ^2/ndp of the integrated cross sections ($\chi^2/ndp|_{\sqrt{s}}^{\pi^-,p}$) are now larger since these data are not included in the global fit.

Table III also shows the newly fitted LDMEs. In comparison with the “REF” calculation, the “FIT” results give smaller $\langle \mathcal{O}_8^H [^3S_1] \rangle$ values for both SMRS and GRV PDFs, while the corresponding Δ_8^H LDMEs are slightly larger. For the JAM and xFitter PDFs the “REF” and “FIT” LDMEs remain consistent within their uncertainties. The $\chi^2/ndp|_{x_F, \sqrt{s}}^p$ have a mild dependence on the pion PDFs, only through the correla-

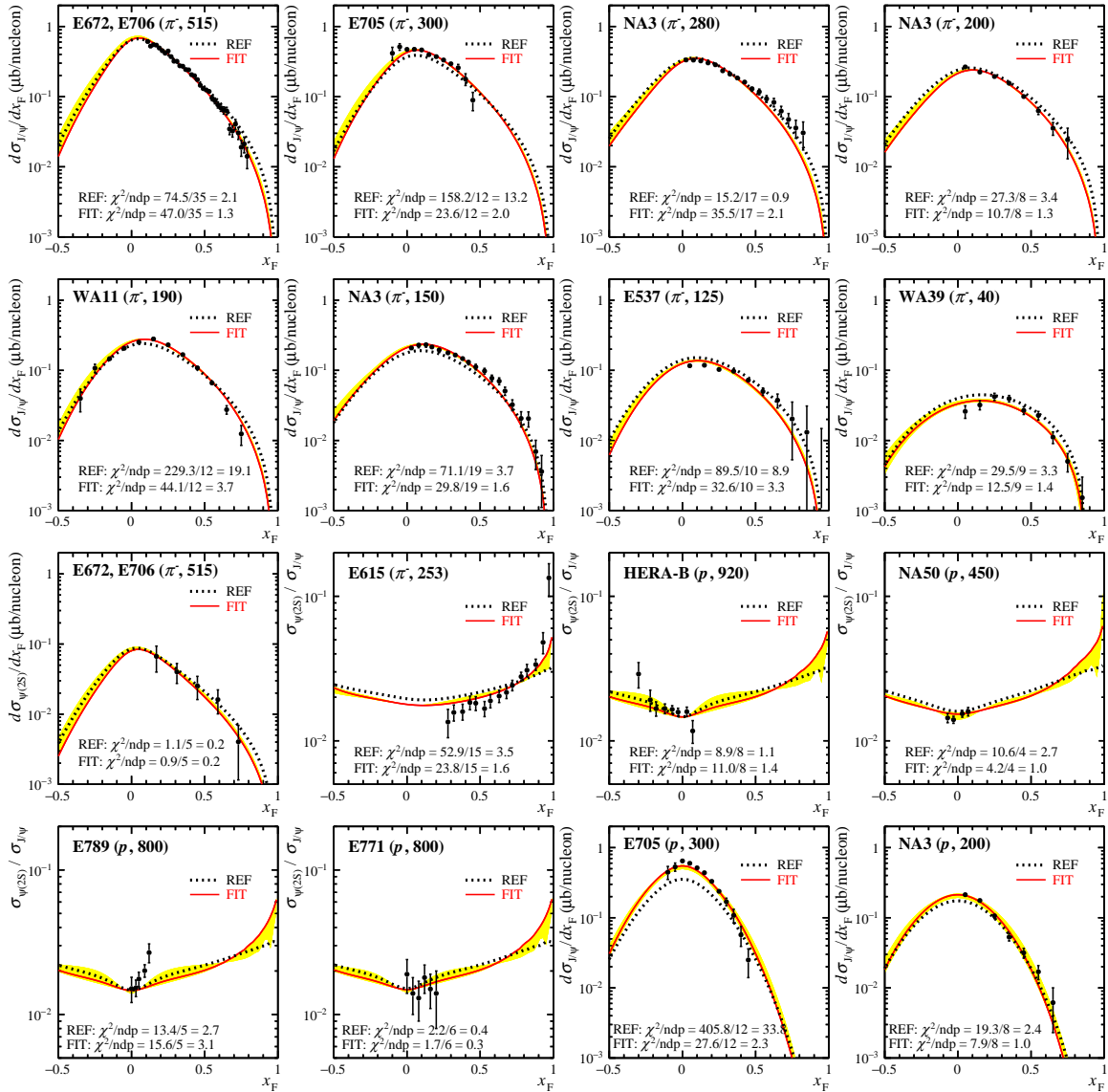


FIG. 2. The x_F -dependent cross sections for J/ψ and $\psi(2S)$ production and $R_\psi(x_F)$ ratios in π^-N and pN interactions, following the order given in Table II. The symbol and value in parenthesis denote the particle type and momentum of beam. The solid red and dotted black curves represent the NRQCD results of SMRS pion PDFs from the fit described in the text (“FIT”) and from the calculation using the LDMs obtained in Ref. [59] (“REF”), respectively. The values of χ^2 divided by the number of data point (ndp) for each dataset are also shown. The yellow bands represent the cross section uncertainties associated with the scale and charm quark mass systematic variations.

tion of LDMs and PDFs in the global fit.

In NRQCD, the relative weighting between $q\bar{q}$ and GG subprocesses is set by a convolution of the pQCD partonic cross sections, the associated parton densities, and the LDMs. The F factor does not modify the shape of $d\sigma/dx_F$. Therefore, adequate shapes of $d\sigma/dx_F$ distributions of individual GG and $q\bar{q}$ contributions from NRQCD calculations are required to achieve a reasonable description of the data, particularly for $x_F > 0.5$. Since the partonic cross sections and the nucleon PDFs involved in the calculations of the cross sections remain the same, the variation of the results originates from the difference in the pion PDFs and the LDMs.

C. Differential cross sections for J/ψ

A comparison of the J/ψ production data and the NRQCD calculations in terms of the subprocess contributions has been made for all of the datasets included in the fit. Irrespective of the pion PDFs, the relative weighting of $q\bar{q}$ and GG shows a strong energy dependence. At the lowest energy, the $q\bar{q}$ term provides the major contribution to the cross section, similar to the DY production, while the GG contribution is dominant at the highest beam energies. A global analysis of charmonium datasets with a wide range of beam energy could simultaneously constrain both pion’s valence quark and gluon distribu-

Data	SMRS		GRV		JAM		xFitter	
	Exp	χ^2/ndp	F	χ^2/ndp	F	χ^2/ndp	F	χ^2/ndp
E672, E706 ($\sigma^{J/\psi}$)	1.3	0.80 ± 0.01	2.6	0.79 ± 0.01	6.1	1.14 ± 0.01	4.2	1.08 ± 0.02
E705 ($\sigma^{J/\psi}$)	2.0	0.98 ± 0.02	1.7	0.96 ± 0.02	4.1	1.19 ± 0.01	2.6	1.18 ± 0.01
NA3 ($\sigma^{J/\psi}$)	2.1	0.86 ± 0.02	2.3	0.87 ± 0.02	2.7	1.00 ± 0.02	2.9	1.01 ± 0.02
NA3 ($\sigma^{J/\psi}$)	1.3	0.87 ± 0.02	0.9	0.89 ± 0.02	1.8	0.92 ± 0.02	1.5	0.95 ± 0.02
WA11 ($\sigma^{J/\psi}$)	3.7	1.02 ± 0.02	8.5	1.02 ± 0.02	29.9	1.09 ± 0.01	22.0	1.12 ± 0.02
NA3 ($\sigma^{J/\psi}$)	1.6	1.24 ± 0.03	1.3	1.23 ± 0.03	1.5	1.10 ± 0.02	1.6	1.18 ± 0.03
E537 ($\sigma^{J/\psi}$)	3.3	0.88 ± 0.00	1.6	0.88 ± 0.01	2.6	0.88 ± 0.00	2.1	0.88 ± 0.01
WA39 ($\sigma^{J/\psi}$)	1.4	1.30 ± 0.04	1.4	1.18 ± 0.07	2.9	0.70 ± 0.00	1.3	0.70 ± 0.05
E672, E706 ($\sigma^{\psi(2S)}$)	0.2	0.80 ± 0.01	0.2	0.79 ± 0.01	0.3	1.14 ± 0.01	0.2	1.08 ± 0.02
E615 ($\sigma^{\psi(2S)}/\sigma^{J/\psi}$)	1.6	1 ± 0	1.7	1 ± 0	5.0	1 ± 0	4.3	1 ± 0
HERA-B ($\sigma^{\psi(2S)}/\sigma^{J/\psi}$)	1.4	1 ± 0	1.5	1 ± 0	1.2	1 ± 0	1.2	1 ± 0
NA50 ($\sigma^{\psi(2S)}/\sigma^{J/\psi}$)	1.0	1 ± 0	1.6	1 ± 0	1.3	1 ± 0	1.1	1 ± 0
E789 ($\sigma^{\psi(2S)}/\sigma^{J/\psi}$)	3.1	1 ± 0	3.3	1 ± 0	2.8	1 ± 0	2.9	1 ± 0
E771 ($\sigma^{\psi(2S)}/\sigma^{J/\psi}$)	0.3	1 ± 0	0.3	1 ± 0	0.3	1 ± 0	0.3	1 ± 0
E705 ($\sigma^{J/\psi}$)	2.3	1.20 ± 0.00	2.2	1.20 ± 0.00	5.7	1.20 ± 0.00	3.1	1.20 ± 0.00
NA3 ($\sigma^{J/\psi}$)	1.0	1.00 ± 0.01	1.2	1.00 ± 0.01	1.9	1.00 ± 0.01	1.6	1.00 ± 0.01

TABLE IV. Results of the NRQCD fits. The columns display the χ^2/ndp values and fitted normalization factors F for each of the selected datasets and for SMRS, GRV, JAM and xFitter pion PDFs.

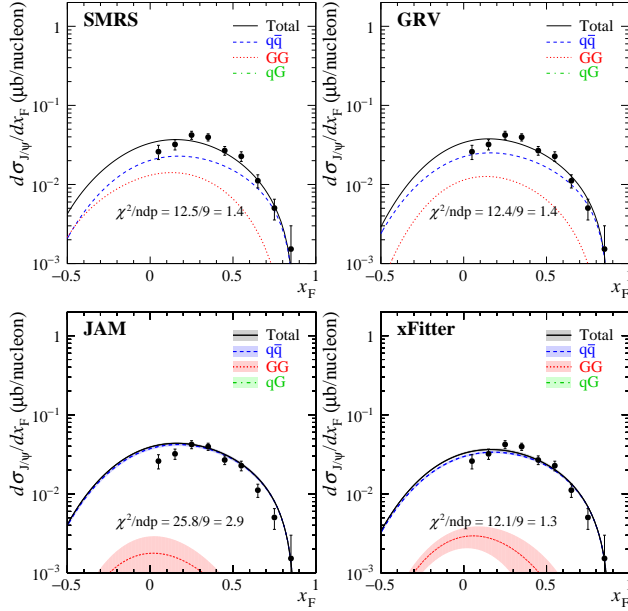


FIG. 3. Differential cross sections for J/ψ production with a 39.5-GeV/ c π^- beam [87]. The data are compared to the NRQCD fit results for the SMRS, GRV, xFitter, and JAM PDFs. The total cross sections and $q\bar{q}$, GG , and qG contributions are denoted as solid black, dashed blue, dotted red, and dot-dashed green lines, respectively. The uncertainty bands associated with JAM and xFitter PDFs are also shown.

tions. It is instructive to compare the results obtained with each of the four pion PDFs. This comparison is illustrated in Figs. 3 and 4 for the data with pion beam momenta of 39.5

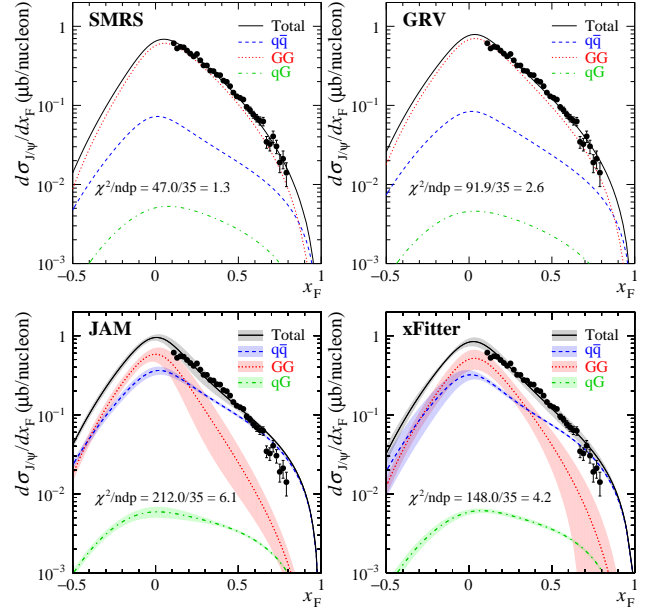


FIG. 4. Same as Fig. 4 for J/ψ production data with a 515 GeV/ c π^- beam [82].

GeV/ c [87] and 515 GeV/ c [82]. The χ^2/ndf values are displayed in the plots.

At the lowest beam momentum of 39.5 GeV/ c (Fig. 3), the $q\bar{q}$ subprocess provides the largest contribution to the cross section over the whole x_F region. The GG contribution is much reduced, so that the shape of the x_F distribution is essentially determined by the shape of the $q\bar{q}$ contribution. Since the pion valence-quark distribution is well determined from

the DY data, good χ^2/ndf values are obtained for the four PDFs. Nevertheless, the agreement with the data is less satisfactory for JAM. Figure 3 also suggests that future J/ψ data at negative x_F with low beam energies could further constrain the pion valence-quark distribution at lower x .

At the highest beam momentum of 515 GeV/c, where the GG contribution becomes dominant, Fig. 4 shows that SMRS and GRV are favored over JAM and xFitter. The fraction of the GG component is maximized around $x_F = 0$, corresponding to the gluon distribution $G_\pi(x)$ around $x \sim 0.1-0.2$. As a result of the rapid drop of the $G_\pi(x)$ toward $x = 1$, the GG contribution quickly decreases at large x_F . In contrast, the $q\bar{q}$ contribution has a slower fall-off toward high x_F because of a relatively strong pion valence antiquark density, in comparison with the gluon one, at large x . Consequently, the $q\bar{q}$ contribution has a broader x_F distribution than that of the GG contribution and the relative importance of $q\bar{q}$ rises at the large x_F region. The ratio of $q\bar{q}$ to GG shows a strong x_F dependence, making the x_F -differential cross sections at high energies particularly sensitive to the shape of pion $G_\pi(x)$.

Similar conclusions can be drawn for the intermediate energies used in this analysis. The corresponding figures are available in the Supplemental Material [92]. As a general observation, the $q\bar{q}$ and GG contributions have quite similar strengths for the fits with SMRS and GRV, whereas the $q\bar{q}$ contribution is the dominant component for the fits with JAM and xFitter. In terms of χ^2/ndf , the data show a slight preference for GRV and SMRS.

D. Differential cross sections for $\psi(2S)$ and the $R_\psi(x_F)$ ratios

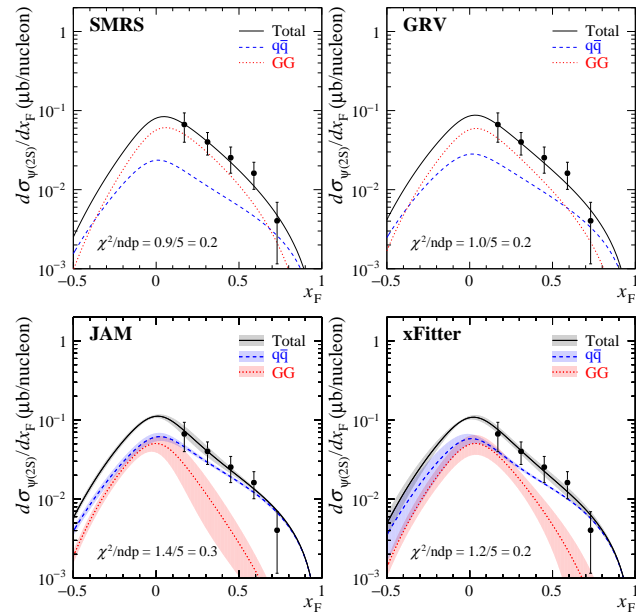


FIG. 5. Same as Fig. 4 for $\psi(2S)$ production with a 515-GeV/c π^- beam [82].

Additional information on the charmonium production mechanism can be obtained by comparing the production of the two charmonium states, J/ψ and $\psi(2S)$. The strengths of their $q\bar{q}$ and GG subprocesses are controlled by the associated LDMEs. In comparison with the J/ψ , the smaller cross section for the $\psi(2S)$ production implies also smaller LDMEs. The fitted LDMEs are indeed smaller, but interestingly, not in the same proportion. As shown in Table III, the values of the $\langle \mathcal{O}_8^{\psi(2S)} [^3S_1] \rangle$ LDMEs for $\psi(2S)$ are smaller than that for J/ψ by about a factor of two. In contrast, the $\Delta_8^{\psi(2S)}$ values for $\psi(2S)$ are an order of magnitude smaller. This is illustrated in Fig. 5 for the E672/E706 $\psi(2S)$ data taken at 515 GeV/c [82]. In comparison with the production of J/ψ at the same energy (Fig. 4), the $q\bar{q}$ contribution is greatly enhanced in $\psi(2S)$ production. Figure 5 shows that this observation is valid for all pion PDFs, and the $q\bar{q}$ term is even dominant for JAM and xFitter. For the fit with the SMRS pion PDFs around $x_F = 0$, the $q\bar{q}$ component accounts for about 15% of the direct part (feed-down excluded) of the J/ψ cross section. Its fraction rises to nearly 30% for $\psi(2S)$. Obviously, the increase of the $q\bar{q}$ term is compensated by a decrease of the GG term. This significant difference between the two charmonium states can only be partially explained by the larger $\psi(2S)$ mass. Its full understanding would require further investigations.

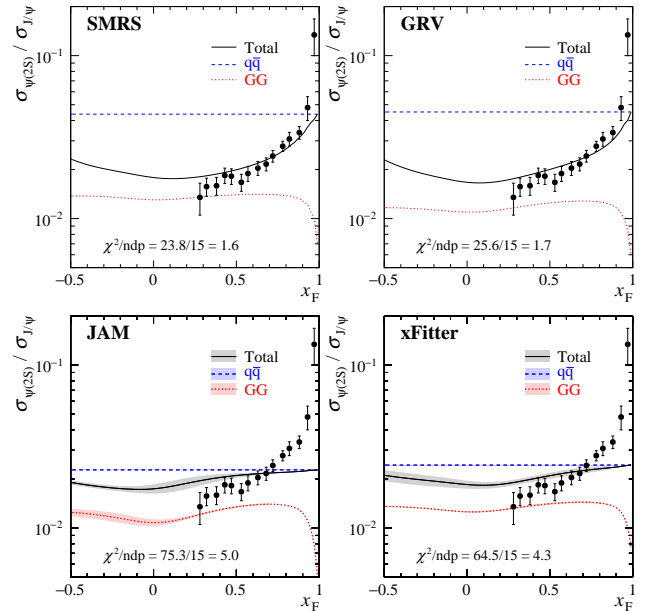


FIG. 6. The $\psi(2S)$ to J/ψ cross section ratios $R_\psi(x_F)$ for J/ψ and $\psi(2S)$ production with a 252-GeV/c π^- beam [88]. The data are compared to the NRQCD fit results for the SMRS, GRV, xFitter, and JAM PDFs. The ratios of total cross sections and individual $R_\psi^{q\bar{q}}(x_F)$ and $R_\psi^{GG}(x_F)$ contributions are denoted as solid black, dashed blue, and dotted red lines, respectively.

The observations above are consistent with the measurements of the $\psi(2S)$ to J/ψ ratios, $R_\psi(x_F)$. The largest statistics on $R_\psi(x_F)$ have been collected by the E615 experiment

for an incident pion momentum of 252 GeV/c [88]. The data are compared to the NRQCD fits with each of the four pion PDFs in Fig. 6. The $R_\psi(x_F)$ shows a strong x_F dependence and this suggests that the relative weights of the individual subprocesses $q\bar{q}$ and GG components in J/ψ and $\psi(2S)$ production are distinctly different. We note that the CEM models predicts an x_F -independent $R_\psi(x_F)$ [78], since the fractions of $q\bar{q}$ and GG components are identical for each charmonium state. In NRQCD, an x_F -dependent $R_\psi(x_F)$ is possible due to the different LDMEs associated with the $q\bar{q}$ and GG channels in producing J/ψ and $\psi(2S)$. The pronounced x_F dependence of $R_\psi(x_F)$ in Fig. 6 clearly disfavors the CEM model.

As shown in Figs. 4 and 5, the $q\bar{q}$ subprocess gives a significantly broader x_F distribution than the GG subprocess. This is caused by the slower fall-off of the valence-quark distribution than the gluon distribution toward $x = 1$. Therefore, the pronounced rise in the $R_\psi(x_F)$ data at forward x_F , shown in Fig. 6, clearly indicates that the $q\bar{q}$ subprocess is more important for the $\psi(2S)$ production than for the J/ψ production.

It is also instructive to examine the x_F dependence of $R_\psi(x_F)$ from the $q\bar{q}$ and GG subprocesses separately. In Fig. 6, the dashed blue and dotted red curves correspond, respectively, to

$$R_\psi^{q\bar{q}}(x_F) \equiv \frac{\sigma_{\psi(2S)}^{q\bar{q}}(x_F)}{\sigma_{J/\psi}^{q\bar{q}}(x_F)}; \quad R_\psi^{GG}(x_F) \equiv \frac{\sigma_{\psi(2S)}^{GG}(x_F)}{\sigma_{J/\psi}^{GG}(x_F)}, \quad (6)$$

where the superscripts $q\bar{q}$ and GG denote the two subprocesses. Neglecting the tiny contribution from the qG subprocess, one can then obtain

$$R_\psi(x_F) \equiv \frac{\sigma_{\psi(2S)}(x_F)}{\sigma_{J/\psi}(x_F)} = [A(x_F)R_\psi^{q\bar{q}}(x_F) + B(x_F)R_\psi^{GG}(x_F)], \quad (7)$$

where

$$A(x_F) = \frac{\sigma_{J/\psi}^{q\bar{q}}(x_F)}{\sigma_{J/\psi}(x_F)} \quad \text{and} \quad B(x_F) = \frac{\sigma_{J/\psi}^{GG}(x_F)}{\sigma_{J/\psi}(x_F)}$$

have the property $0 \leq A(x_F) \leq 1$ and $0 \leq B(x_F) \leq 1$. It follows that $R_\psi(x_F)$ must be bounded by $R_\psi^{GG}(x_F)$ and $R_\psi^{q\bar{q}}(x_F)$ in Fig. 6. As shown in Fig. 6, the $R_\psi(x_F)$ data largely fall within these two bounds for calculations with the SMRS and GRV PDFs, while a large fraction of the data are outside of these bounds for the calculations using the JAM and xFitter PDFs. The striking contrast between the SMRS/GRV and the JAM/xFitter PDFs in their ability to describe the $R_\psi(x_F)$ data in Fig. 6 illustrates the advantages of the $R_\psi(x_F)$ data in constraining the pion PDFs. We also note that none of the pion PDFs can explain the sharp rise of the $R_\psi(x_F)$ data beyond $x_F = 0.8$. This incompatibility at large x_F could be due to either higher-twist effects [88] or higher-order QCD processes that are beyond the present leading-order NRQCD analysis.

Our analysis also shows that fixed-target charmonium production data are particularly sensitive to the color octet contribution to the cross section. This is illustrated in Fig. 7 which

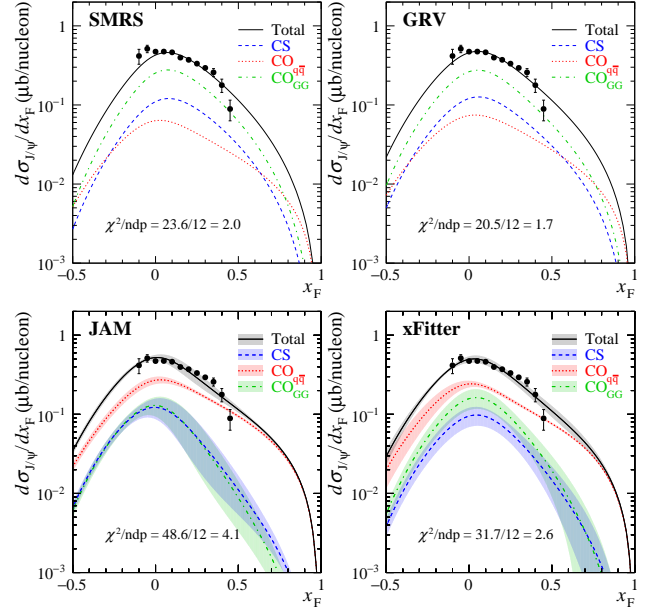


FIG. 7. Differential cross sections for J/ψ production with a 300 GeV/c π^- beam [83]. The data are compared to the fit results with SMRS, GRV, xFitter, and JAM PDFs. The total cross section and its decomposition into contributions from CS, CO $q\bar{q}$ and CO GG subprocesses are denoted as solid black, dashed blue, dotted red and dot-dashed green lines, respectively.

displays the decomposition of the J/ψ x_F -dependent cross sections from the E705 experiment [83] into color octet and color singlet contributions. The CO contribution plays a dominant role in the J/ψ production across the entire x_F range, and this observation is valid for any of the four pion PDFs. Further information can be obtained by separating the CO contribution into GG and $q\bar{q}$ components. Only the CO GG component, controlled by the Δ_8^H LDME, is displayed. For the SMRS and GRV pion PDFs it provides the largest part of the CO contribution. In contrast, its relative magnitude is significantly reduced for the JAM and xFitter PDFs, an observation that is in line with their smaller gluon distributions.

E. Integrated cross sections

Because of the presence of valence antiquarks in the pion, the $q\bar{q}$ and GG subprocesses to the J/ψ production with proton and pion beams have different contributions to the integrated cross sections. In the production with a proton beam the GG contribution is dominant across all center-of-mass energies \sqrt{s} except near threshold. With pion beams the $q\bar{q}$ contribution is significantly enhanced. It dominates at low energies, with GG contribution gradually becoming important as \sqrt{s} increases.

Our analysis of the differential cross sections shows that the relative contributions of the $q\bar{q}$ and GG subprocesses in the production of J/ψ and $\psi(2S)$ differ considerably. The same conclusion can be drawn from the integrated cross sec-

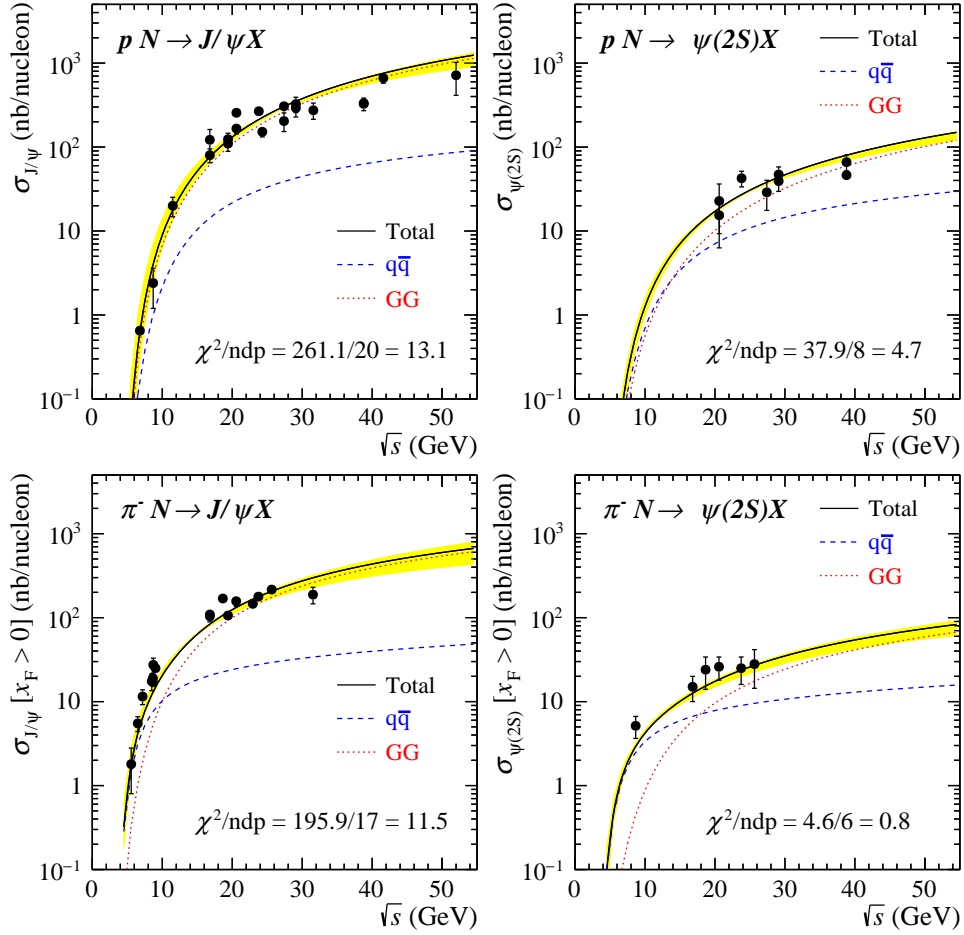


FIG. 8. Integrated charmonium cross sections in pN and $\pi^- N$ collisions. The data for J/ψ and $\psi(2S)$ production are compared to the results of NRQCD calculations with the SMRS pion PDFs and the “FIT” LDMEs in Table III. The total cross section and its $q\bar{q}$ and GG contributions are denoted as solid black, dashed blue and dotted red lines, respectively. The yellow bands represent the cross section uncertainties associated with the scale and charm quark mass systematic variations.

tions. Figure 8 shows the comparison of data and NRQCD calculations for the J/ψ and $\psi(2S)$ production cross sections in pN and $\pi^- N$ collisions with the SMRS pion PDFs and the “FIT” LDMEs in Table III. The fractions of $q\bar{q}$ and GG contributions as a function of \sqrt{s} vary considerably, reflecting the differences of the corresponding gluon and quark parton distributions between the pion PDFs. For SMRS, whose gluon strength at large x is relatively strong, the GG contribution starts to dominate the cross section beyond $\sqrt{s} = 18$ and 10 GeV for the production of $\psi(2S)$ and J/ψ , respectively, while the transition happens at larger \sqrt{s} for the results with JAM, in consequence of a relatively weak gluon strength. The uncertainty bands estimated in the same fashion as in Fig. 2 are displayed. The plots for GRV, JAM and xFitter pion PDFs are provided in the Supplemental Material [92]. All these observations confirm our previous conclusion: the $q\bar{q}$ contribution plays a much more important role in the $\psi(2S)$ production, compared to J/ψ .

F. Systematic studies

So far only the uncertainties associated with the parametrizations of JAM and xFitter PDFs have been taken into account. Our results are also sensitive to the NRQCD input parameters and to the choice of the nuclear PDFs. We have checked that fits performed with the nCTEQ15 [93] parametrization instead of EPPS16 result in negligible differences. Fits with the factorization/renormalization scale parameter μ_R set to 1, 2, and 4 m_c , with $m_c = 1.4, 1.5,$ and 1.6 GeV/c^2 , have also been made. The values of the total χ^2/ndf do not vary much: they remain nearly unchanged between $\mu_R = m_c$ and $\mu_R = 4m_c$ at $m_c = 1.5 \text{ GeV}/c^2$. The effect on the values of the LDMEs is more important. For both J/ψ and $\psi(2S)$ the fitted LDMEs increase by nearly a factor of four when μ_R increases from $\mu_R = m_c$ to $\mu_R = 4m_c$. Nevertheless, the shape and the magnitude of the final cross section remain nearly unchanged, as illustrated in Fig. 9 for the fit with the SMRS PDFs. The relative contributions of the $q\bar{q}$ and GG subprocesses for the three values of μ_R are only

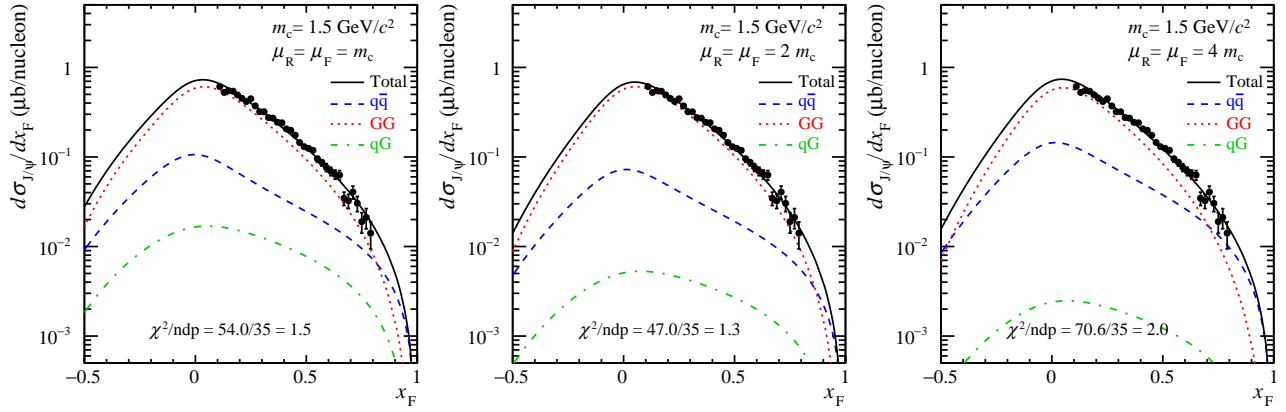


FIG. 9. The NRQCD results with variation of charm quark mass m_c and renormalization scale μ_R , compared with the $d\sigma/dx_F$ data of J/ψ production off the beryllium target with a 515-GeV/c π^- beam from the E672/E706 experiment [82]. The pion PDFs used for the calculation is SMRS. The total cross sections and $q\bar{q}$, GG , and qG contributions are denoted as solid black, dashed blue, dotted red and dot-dashed green lines, respectively. The charm quark mass m_c , factorization scale μ_F , and renormalization scale μ_R used for the NRQCD calculation as well as the fit χ^2/ndf are displayed in each plot.

slightly modified. The charm quark mass correlates with the LDMEs in the partonic cross sections. Consequently, the variation of m_c around its nominal value affects the values of the best-fit LDMEs and the overall quality of fits remains stable. The systematic studies with GRV, JAM and xFitter pion PDFs lead to results fully consistent with these conclusions. The corresponding figures and tables are available in the Supplemental Material [92].

The overall χ^2/ndf for the pion-induced J/ψ and $\psi(2S)$ x_F -dependent data versus different choices of scale and m_c for four pion PDFs are shown in Fig. 10. The χ^2/ndf values of SMRS and GRV remain consistently better than those of JAM and xFitter. The systematic variation of the scale and mass parameters do not change the preference of the data for GRV and SMRS.

In addition, the theoretical uncertainties corresponding to the variations of m_c from 1.4 to 1.6 GeV at $\mu_R = 2 m_c$, and those of μ from m_c to $4 m_c$ at $m_c = 1.5 \text{ GeV}/c^2$ with the fixed LDMEs labeled as ‘‘FIT’’ in Table III for the total and differential x_F cross sections are displayed as yellow bands in Figs. 22 and 23, respectively, in the Supplemental Material [92]. Compared to Figs. 2 and 8, the uncertainty bands in these two additional figures are significantly larger, with the overall χ^2/ndf rising by a factor of 20 to 50. We note however that the increase in χ^2 is primarily due to the changes in the overall normalization, common to all pion PDFs, while the shapes of the x_F dependence are largely preserved. This suggests that the ability to discriminate various pion PDFs, based on their predicted shapes of the x_F distributions, is insensitive to the choice of m_c and μ .

VI. DISCUSSION

Our analysis shows that the x_F -dependent proton and pion-induced J/ψ and $\psi(2S)$ production data can be simultaneously described within the NRQCD framework. The results

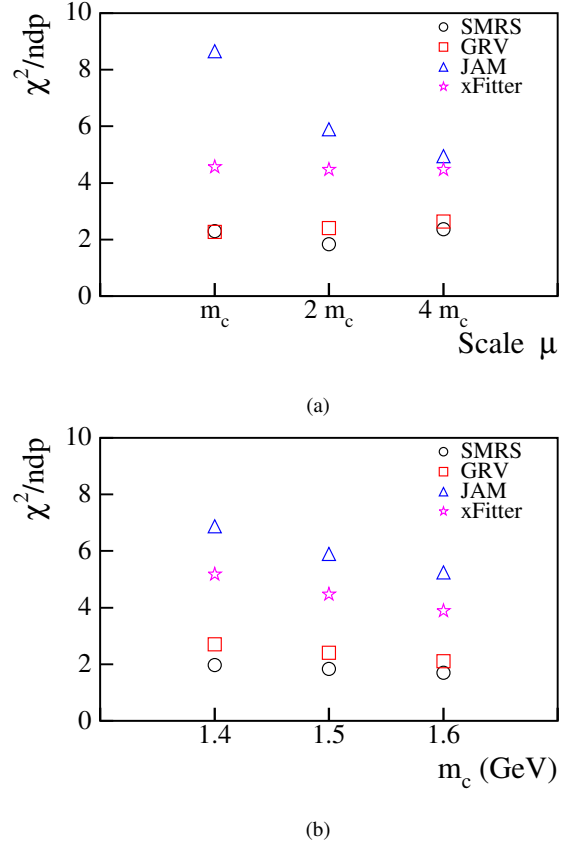


FIG. 10. The χ^2 divided by the number of data point (ndp) of the pion-induced x_F -dependent data for four pion PDFs versus: (a) the scale parameter μ_R (b) and charm mass m_c .

exhibit a strong dependence on the pion PDFs and particularly on the gluon distribution. The conclusions drawn here

fully corroborate the results obtained previously [58] using the more phenomenological color evaporation model. The similarity between the results of the two studies indicate that our main findings are quite independent of the charmonium production models.

We note that our analysis is performed in leading order only and in the region of small p_T , in which a proof of factorization is still lacking. Our work is based on the assumption adopted in Refs. [60] and [74] that NRQCD can lead to a satisfactory description of proton-induced charmonium production at fixed-target energies. In order to evaluate the theoretical uncertainties associated with these limitations, we also investigated the sensitivity of the results to the NRQCD input parameters. Varying the scale and the charm mass parameters within the commonly accepted ranges leads to the error bands shown in Figs. 2 and 8. The calculations with each of the four pion PDFs are all modified consistently, preserving the dependence already observed for the best fits.

The values of the color-octet LDMEs, resulting from the fits to the data may contain model uncertainties, although they provide a good description of the data. The formalism used is limited to LO and is able to determine individually the CO $\langle \mathcal{O}_8^H [^3S_1] \rangle$ LDMEs for J/ψ and $\psi(2S)$ only. The $\Delta_8^{J/\psi}$ and $\Delta_8^{\psi(2S)}$ terms combine each three additional color octet LDMEs. Furthermore, most of the data included in the analysis have transverse momenta p_T smaller than 3 GeV/ c . This is in sharp contrast with most of the available LDMEs that result from fits at much larger energies and for transverse momenta p_T larger than 5 GeV/ c [94] and often even larger than 10 GeV/ c [95]. Assuming the approximate universality of the LDMEs, a comparison with the published values remains qualitative and can be solely used as an indirect criterion for the significance of our results [96].

For the fits on the J/ψ data sample, the $\langle \mathcal{O}_8^{J/\psi} [^3S_1] \rangle$ values obtained, e.g. $(2.59 \pm 0.23) \times 10^{-2} \text{ GeV}^3$ for the SMRS pion PDFs, are nearly an order of magnitude larger than some of the published LDMEs [97, 98]. Yet, they are only a factor of 2.5 larger than the values of $(1.0 \pm 0.3) \times 10^{-2} \text{ GeV}^3$ reported in Ref. [99] derived from data on η_c production using spin symmetry relations and $(1.1 \pm 1.0) \times 10^{-2} \text{ GeV}^3$ obtained in Ref. [95] from fits to Tevatron and LHC data. For the $\psi(2S)$, the fitted $\langle \mathcal{O}_8^{\psi(2S)} [^3S_1] \rangle$ LDME with the SMRS pion PDFs has a value of $(1.32 \pm 0.90) \times 10^{-2} \text{ GeV}^3$, about a factor of four larger than the values quoted in Refs. [100, 101] and more recently in Ref. [102]. A value with a different sign has also been reported [103]. The comparison of our $\Delta_8^{J/\psi}$ and $\Delta_8^{\psi(2S)}$ LDMEs with the individual CO $\langle \mathcal{O}_8^{J/\psi} [^1S_0] \rangle$ values is only indicative. The $\Delta_8^{J/\psi}$ value is compatible with the values derived in Refs. [95, 97–99]. The $\Delta_8^{\psi(2S)}$ LDME is also inside the range defined by the values quoted in Refs. [100–102]. Within the systematic uncertainties associated with the fits and given the assumptions made, the comparison can be considered satisfactory, providing an indirect support for the present analysis.

Our analysis is performed using a leading-order NRQCD framework only. The results obtained may vary if a more advanced NRQCD formalism with higher order terms is ap-

plied. In addition, for most of the fixed-target data considered here, the mean transverse momenta are smaller than the J/ψ mass. Inclusion of higher-order corrections could therefore provide a better description, but probably would not change the general conclusions. The analysis has been also limited to data taken with only light targets. A large amount of data of x_F -differential cross sections with heavier targets have been collected in the past. These data could be included in a more complete analysis if the energy loss effects [104] responsible for the suppression of the charmonium cross section in hadron-nucleus collisions are reliably accounted for.

VII. CONCLUSION

We have analyzed fixed-target experimental cross sections for J/ψ and $\psi(2S)$ production using the NRQCD framework. To minimize nuclear matter effects, only data on hydrogen, lithium and beryllium targets were selected. Heavier targets were only considered for the data on the J/ψ to $\psi(2S)$ ratios. Assuming the universality of the NRQCD approach, both pion and proton-induced datasets were included in the analysis. Fits to the individual x_F -differential cross sections and their ratios have been made, using four different pion PDF parametrizations. The proton data, although not directly sensitive to the pion PDFs, enrich the selection and contribute to the stability of the final results.

A simultaneous fit to all pion and proton datasets has been achieved. The results of these common fits show that the relative fractions of the $q\bar{q}$ and GG contributions to the cross sections strongly depend on the beam particle, on its incoming energy and on the x_F region considered. A strong dependence on the pion PDF parametrization used is observed and particularly on the magnitude of the pion gluon distribution. The results indicate a clear preference for parametrizations with larger gluon distributions at relatively large x . Good agreement with the data is obtained with the SMRS and GRV PDFs. The fits with the recent JAM and xFitter parametrizations turn out to show much larger deviations for most of the datasets.

The comparison between the results for J/ψ and $\psi(2S)$ production leads to an important new observation: the strengths of the $q\bar{q}$ and GG contributions to these two charmonium states are – unexpectedly – quite different. The $q\bar{q}$ component of the $\psi(2S)$ cross section is, proportionally, few times larger than the $q\bar{q}$ component of the J/ψ cross section. This interesting feature is confirmed for both differential and integrated cross sections and for both pion and proton beams. The production of $\psi(2S)$ appears to be more sensitive to the pion’s valence quark distribution than that of J/ψ . This observation could be relevant for a better understanding of the charmonium production mechanism.

In the kinematical domain of the available fixed-target data – relatively small center-of-mass energy and therefore small transverse momenta – the theoretical uncertainties could be substantial. A proof of factorization is still lacking and additional higher-order corrections may play a role. Conversely, the conclusions drawn rely on a simultaneous study of the pion and proton-induced cross sections and ratios, both x_F -

differential and integrated, for all of which the agreement achieved is quite good. The conclusions are also fully supported by the results from our previous study done with the color evaporation model [58]. While further theoretical efforts are required to better understand the reaction mechanism for quarkonium production, the inclusion of the charmonium data in a new global analysis to extract the pion PDFs would be very informative [105].

New results of Drell-Yan as well as J/ψ measurements in πA reactions will be available from the CERN COMPASS [106] and AMBER [107] experiments in the near future. These data will be important in providing better knowledge

of the pion PDFs. For the longer-term electron-ion collider projects in U.S. and China, the pion as well kaon structures are planned to be explored using the tagged DIS process [108–110].

ACKNOWLEDGMENTS

This work was supported in part by the U.S. National Science Foundation and National Science and Technology Council of Taiwan (R.O.C.).

-
- [1] T. Horn and C. D. Roberts, *J. Phys. G* **43**, 073001 (2016), arXiv:1602.04016 [nucl-th].
- [2] S.-i. Nam, *Phys. Rev. D* **86**, 074005 (2012), arXiv:1205.4156 [hep-ph].
- [3] A. Watanabe, C. W. Kao, and K. Suzuki, *Phys. Rev. D* **94**, 114008 (2016), arXiv:1610.08817 [hep-ph].
- [4] A. Watanabe, T. Sawada, and C. W. Kao, *Phys. Rev. D* **97**, 074015 (2018), arXiv:1710.09529 [hep-ph].
- [5] P. T. P. Hutaauruk, I. C. Cloet, and A. W. Thomas, *Phys. Rev. C* **94**, 035201 (2016), arXiv:1604.02853 [nucl-th].
- [6] J. Lan, C. Mondal, S. Jia, X. Zhao, and J. P. Vary, *Phys. Rev. Lett.* **122**, 172001 (2019), arXiv:1901.11430 [nucl-th].
- [7] J. Lan, C. Mondal, S. Jia, X. Zhao, and J. P. Vary, *Phys. Rev. D* **101**, 034024 (2020), arXiv:1907.01509 [nucl-th].
- [8] J. Lan, K. Fu, C. Mondal, X. Zhao, and J. P. Vary (BLFQ), *Phys. Lett. B* **825**, 136890 (2022), arXiv:2106.04954 [hep-ph].
- [9] G. F. de Teramond, T. Liu, R. S. Sufian, H. G. Dosch, S. J. Brodsky, and A. Deur (HLFHS), *Phys. Rev. Lett.* **120**, 182001 (2018), arXiv:1801.09154 [hep-ph].
- [10] A. Watanabe, T. Sawada, and M. Huang, *Phys. Lett. B* **805**, 135470 (2020), arXiv:1910.10008 [hep-ph].
- [11] J. Lan and C. Mondal, *Phys. Lett. B* **807**, 135613 (2020), arXiv:2007.05858 [hep-ph].
- [12] C. Han, H. Xing, X. Wang, Q. Fu, R. Wang, and X. Chen, *Phys. Lett. B* **800**, 135066 (2020), arXiv:1809.01549 [hep-ph].
- [13] C. Han, G. Xie, R. Wang, and X. Chen, *Eur. Phys. J. C* **81**, 302 (2021), arXiv:2010.14284 [hep-ph].
- [14] L. Chang, C. Mezrag, H. Moutarde, C. D. Roberts, J. Rodríguez-Quintero, and P. C. Tandy, *Phys. Lett. B* **737**, 23 (2014), arXiv:1406.5450 [nucl-th].
- [15] L. Chang and A. W. Thomas, *Phys. Lett. B* **749**, 547 (2015), arXiv:1410.8250 [nucl-th].
- [16] C. Chen, L. Chang, C. D. Roberts, S. Wan, and H.-S. Zong, *Phys. Rev. D* **93**, 074021 (2016), arXiv:1602.01502 [nucl-th].
- [17] C. Shi, C. Mezrag, and H.-s. Zong, *Phys. Rev. D* **98**, 054029 (2018), arXiv:1806.10232 [nucl-th].
- [18] K. D. Bednar, I. C. Cloët, and P. C. Tandy, *Phys. Rev. Lett.* **124**, 042002 (2020), arXiv:1811.12310 [nucl-th].
- [19] M. Ding, K. Raya, D. Binosi, L. Chang, C. D. Roberts, and S. M. Schmidt, *Phys. Rev. D* **101**, 054014 (2020), arXiv:1905.05208 [nucl-th].
- [20] Z.-F. Cui, M. Ding, F. Gao, K. Raya, D. Binosi, L. Chang, C. D. Roberts, J. Rodríguez-Quintero, and S. M. Schmidt, *Eur. Phys. J. C* **80**, 1064 (2020).
- [21] A. Freese, I. C. Cloët, and P. C. Tandy, *Phys. Lett. B* **823**, 136719 (2021), arXiv:2103.05839 [hep-ph].
- [22] L. Chang and C. D. Roberts, *Chin. Phys. Lett.* **38**, 081101 (2021), arXiv:2106.08451 [hep-ph].
- [23] Z. F. Cui, M. Ding, J. M. Morgado, K. Raya, D. Binosi, L. Chang, J. Papavassiliou, C. D. Roberts, J. Rodríguez-Quintero, and S. M. Schmidt, *Eur. Phys. J. A* **58**, 10 (2022), arXiv:2112.09210 [hep-ph].
- [24] Z. F. Cui, M. Ding, J. M. Morgado, K. Raya, D. Binosi, L. Chang, F. De Soto, C. D. Roberts, J. Rodríguez-Quintero, and S. M. Schmidt, *Phys. Rev. D* **105**, L091502 (2022), arXiv:2201.00884 [hep-ph].
- [25] J.-H. Zhang, J.-W. Chen, L. Jin, H.-W. Lin, A. Schäfer, and Y. Zhao, *Phys. Rev. D* **100**, 034505 (2019), arXiv:1804.01483 [hep-lat].
- [26] R. S. Sufian, J. Karpie, C. Egerer, K. Orginos, J.-W. Qiu, and D. G. Richards, *Phys. Rev. D* **99**, 074507 (2019), arXiv:1901.03921 [hep-lat].
- [27] T. Izubuchi, L. Jin, C. Kallidonis, N. Karthik, S. Mukherjee, P. Petreczky, C. Shugert, and S. Syritsyn, *Phys. Rev. D* **100**, 034516 (2019), arXiv:1905.06349 [hep-lat].
- [28] B. Joó, J. Karpie, K. Orginos, A. V. Radyushkin, D. G. Richards, R. S. Sufian, and S. Zafeiropoulos, *Phys. Rev. D* **100**, 114512 (2019), arXiv:1909.08517 [hep-lat].
- [29] R. S. Sufian, C. Egerer, J. Karpie, R. G. Edwards, B. Joó, Y.-Q. Ma, K. Orginos, J.-W. Qiu, and D. G. Richards, *Phys. Rev. D* **102**, 054508 (2020), arXiv:2001.04960 [hep-lat].
- [30] J.-W. Chen, H.-W. Lin, and J.-H. Zhang, *Nucl. Phys. B* **952**, 114940 (2020), arXiv:1904.12376 [hep-lat].
- [31] X. Gao, L. Jin, C. Kallidonis, N. Karthik, S. Mukherjee, P. Petreczky, C. Shugert, S. Syritsyn, and Y. Zhao, *Phys. Rev. D* **102**, 094513 (2020), arXiv:2007.06590 [hep-lat].
- [32] C. Alexandrou, S. Bacchio, I. Cloet, M. Constantinou, K. Hadjiyiannakou, G. Koutsou, and C. Lauer (ETM), *Phys. Rev. D* **103**, 014508 (2021), arXiv:2010.03495 [hep-lat].
- [33] C. Alexandrou, S. Bacchio, I. Cloët, M. Constantinou, K. Hadjiyiannakou, G. Koutsou, and C. Lauer (ETM), *Phys. Rev. D* **104**, 054504 (2021), arXiv:2104.02247 [hep-lat].
- [34] Z. Fan and H.-W. Lin, *Phys. Lett. B* **823**, 136778 (2021), arXiv:2104.06372 [hep-lat].
- [35] W. Detmold, A. V. Grebe, I. Kanamori, C. J. D. Lin, S. Mondal, R. J. Perry, and Y. Zhao (HOPE), *Phys. Rev. D* **105**, 034506 (2022), arXiv:2109.15241 [hep-lat].
- [36] X. Gao, A. D. Hanlon, N. Karthik, S. Mukherjee, P. Petreczky, P. Scior, S. Shi, S. Syritsyn, Y. Zhao, and K. Zhou, (2022), arXiv:2208.02297 [hep-lat].
- [37] P. C. Barry *et al.* (Jefferson Lab Angular Momentum (JAM), HadStruc), *Phys. Rev. D* **105**, 114051 (2022),

- arXiv:2204.00543 [hep-ph].
- [38] W.-C. Chang and D. Dutta, *Int. J. Mod. Phys. E* **22**, 1330020 (2013), arXiv:1306.3971 [nucl-th].
- [39] J. T. Londergan, G. Q. Liu, E. N. Rodionov, and A. W. Thomas, *Phys. Lett. B* **361**, 110 (1995).
- [40] M. Bonesini *et al.* (WA70), *Z. Phys. C* **37**, 535 (1988).
- [41] V. A. Khoze, A. D. Martin, and M. G. Ryskin, *Eur. Phys. J. C* **48**, 797 (2006), arXiv:hep-ph/0606213.
- [42] J. R. McKenney, N. Sato, W. Melnitchouk, and C.-R. Ji, *Phys. Rev. D* **93**, 054011 (2016), arXiv:1512.04459 [hep-ph].
- [43] M. Gluck, J. F. Owens, and E. Reya, *Phys. Rev. D* **17**, 2324 (1978).
- [44] V. D. Barger, W.-Y. Keung, and R. J. N. Phillips, *Z. Phys. C* **6**, 169 (1980).
- [45] J. F. Owens, *Phys. Rev. D* **30**, 943 (1984).
- [46] N. Brambilla *et al.*, *Eur. Phys. J. C* **71**, 1534 (2011), arXiv:1010.5827 [hep-ph].
- [47] J.-P. Lansberg, *Phys. Rept.* **889**, 1 (2020), arXiv:1903.09185 [hep-ph].
- [48] M. B. Einhorn and S. D. Ellis, *Phys. Rev. D* **12**, 2007 (1975).
- [49] H. Fritzsch, *Phys. Lett. B* **67**, 217 (1977).
- [50] F. Halzen, *Phys. Lett. B* **69**, 105 (1977).
- [51] C.-H. Chang, *Nucl. Phys. B* **172**, 425 (1980).
- [52] E. L. Berger and D. L. Jones, *Phys. Rev. D* **23**, 1521 (1981).
- [53] R. Baier and R. Ruckl, *Z. Phys. C* **19**, 251 (1983).
- [54] G. T. Bodwin, E. Braaten, and G. P. Lepage, *Phys. Rev. D* **51**, 1125 (1995), [Erratum: *Phys.Rev.D* 55, 5853 (1997)], arXiv:hep-ph/9407339.
- [55] G. T. Bodwin, E. Braaten, and J. Lee, *Phys. Rev. D* **72**, 014004 (2005), arXiv:hep-ph/0504014.
- [56] G. A. Schuler, *Quarkonium production and decays*, Ph.D. thesis, Hamburg U. (1994), arXiv:hep-ph/9403387.
- [57] R. Vogt, *Phys. Rept.* **310**, 197 (1999).
- [58] W.-C. Chang, J.-C. Peng, S. Platchkov, and T. Sawada, *Phys. Rev. D* **102**, 054024 (2020), arXiv:2006.06947 [hep-ph].
- [59] C.-Y. Hsieh, Y.-S. Lian, W.-C. Chang, J.-C. Peng, S. Platchkov, and T. Sawada, *Chin. J. Phys.* **73**, 13 (2021), arXiv:2103.11660 [hep-ph].
- [60] M. Beneke and I. Z. Rothstein, *Phys. Rev. D* **54**, 2005 (1996), [Erratum: *Phys.Rev.D* 54, 7082 (1996)], arXiv:hep-ph/9603400.
- [61] P. C. Barry, N. Sato, W. Melnitchouk, and C.-R. Ji, *Phys. Rev. Lett.* **121**, 152001 (2018), arXiv:1804.01965 [hep-ph].
- [62] N. Y. Cao, P. C. Barry, N. Sato, and W. Melnitchouk (Jefferson Lab Angular Momentum), *Phys. Rev. D* **103**, 114014 (2021), arXiv:2103.02159 [hep-ph].
- [63] P. C. Barry, C.-R. Ji, N. Sato, and W. Melnitchouk (Jefferson Lab Angular Momentum (JAM)), *Phys. Rev. Lett.* **127**, 232001 (2021), arXiv:2108.05822 [hep-ph].
- [64] I. Novikov *et al.*, *Phys. Rev. D* **102**, 014040 (2020), arXiv:2002.02902 [hep-ph].
- [65] P. J. Sutton, A. D. Martin, R. G. Roberts, and W. J. Stirling, *Phys. Rev. D* **45**, 2349 (1992).
- [66] M. Gluck, E. Reya, and A. Vogt, *Z. Phys. C* **53**, 651 (1992).
- [67] M. R. Whalley, D. Bourilkov, and R. C. Group, in *HERA and the LHC: A Workshop on the Implications of HERA and LHC Physics (Startup Meeting, CERN, 26-27 March 2004; Midterm Meeting, CERN, 11-13 October 2004)* (2005) pp. 575–581, arXiv:hep-ph/0508110.
- [68] A. Buckley, J. Ferrando, S. Lloyd, K. Nordström, B. Page, M. Rüfenacht, M. Schönherr, and G. Watt, *Eur. Phys. J. C* **75**, 132 (2015), arXiv:1412.7420 [hep-ph].
- [69] P. Nason, S. Dawson, and R. K. Ellis, *Nucl. Phys. B* **303**, 607 (1988).
- [70] P. Nason, S. Dawson, and R. K. Ellis, *Nucl. Phys. B* **327**, 49 (1989), [Erratum: *Nucl.Phys.B* 335, 260–260 (1990)].
- [71] M. L. Mangano, P. Nason, and G. Ridolfi, *Nucl. Phys. B* **405**, 507 (1993).
- [72] E. J. Eichten and C. Quigg, *Phys. Rev. D* **52**, 1726 (1995), arXiv:hep-ph/9503356.
- [73] R. Vogt, *Phys. Rev. C* **61**, 035203 (2000), arXiv:hep-ph/9907317.
- [74] F. Maltoni *et al.*, *Phys. Lett. B* **638**, 202 (2006), arXiv:hep-ph/0601203.
- [75] P. A. Zyla *et al.* (Particle Data Group), *PTEP* **2020**, 083C01 (2020).
- [76] S. Dulat, T.-J. Hou, J. Gao, M. Guzzi, J. Huston, P. Nadolsky, J. Pumplin, C. Schmidt, D. Stump, and C. P. Yuan, *Phys. Rev. D* **93**, 033006 (2016), arXiv:1506.07443 [hep-ph].
- [77] K. J. Eskola, P. Paakkinen, H. Paukkunen, and C. A. Salgado, *Eur. Phys. J. C* **77**, 163 (2017), arXiv:1612.05741 [hep-ph].
- [78] I. Abt *et al.* (HERA-B), *Eur. Phys. J. C* **49**, 545 (2007), arXiv:hep-ex/0607046.
- [79] C. Baglin *et al.* (NA38), *Phys. Lett. B* **345**, 617 (1995).
- [80] Y. Alexandrov *et al.* (BEATRICE), *Nucl. Phys. B* **557**, 3 (1999).
- [81] M. J. Corden *et al.* (WA39), *Phys. Lett. B* **96**, 411 (1980).
- [82] A. Gribushin *et al.* (E672, E706), *Phys. Rev. D* **53**, 4723 (1996).
- [83] L. Antoniazzi *et al.* (E705), *Phys. Rev. D* **46**, 4828 (1992).
- [84] J. Badier *et al.* (NA3), *Z. Phys. C* **20**, 101 (1983).
- [85] J. G. McEwen *et al.* (WA11), *Phys. Lett. B* **121**, 198 (1983).
- [86] C. Akerlof *et al.* (E537), *Phys. Rev. D* **48**, 5067 (1993).
- [87] M. J. Corden *et al.* (WA39), *Phys. Lett. B* **98**, 220 (1981).
- [88] J. G. Heinrich *et al.* (E615), *Phys. Rev. D* **44**, 1909 (1991).
- [89] B. Alessandro *et al.* (NA50), *Eur. Phys. J. C* **33**, 31 (2004).
- [90] M. H. Schub *et al.* (E789), *Phys. Rev. D* **52**, 1307 (1995), [Erratum: *Phys.Rev.D* 53, 570 (1996)].
- [91] T. Alexopoulos *et al.* (E771), *Phys. Lett. B* **374**, 271 (1996).
- [92] See Supplemental materials for additional results of comparison of data and NRQCD calculations and the systematic studies..
- [93] K. Kovarik *et al.*, *Phys. Rev. D* **93**, 085037 (2016), arXiv:1509.00792 [hep-ph].
- [94] J. P. Lansberg, *Int. J. Mod. Phys. A* **21**, 3857 (2006), arXiv:hep-ph/0602091.
- [95] G. T. Bodwin, H. S. Chung, U.-R. Kim, and J. Lee, *Phys. Rev. Lett.* **113**, 022001 (2014), arXiv:1403.3612 [hep-ph].
- [96] I. Z. Rothstein, *Int. J. Mod. Phys. A* **12**, 3857 (1997), arXiv:hep-ph/9609281.
- [97] M. Butenschoen and B. A. Kniehl, *Phys. Rev. Lett.* **106**, 022003 (2011), arXiv:1009.5662 [hep-ph].
- [98] K.-T. Chao, Y.-Q. Ma, H.-S. Shao, K. Wang, and Y.-J. Zhang, *Phys. Rev. Lett.* **108**, 242004 (2012), arXiv:1201.2675 [hep-ph].
- [99] H.-F. Zhang, Z. Sun, W.-L. Sang, and R. Li, *Phys. Rev. Lett.* **114**, 092006 (2015), arXiv:1412.0508 [hep-ph].
- [100] Y.-Q. Ma, K. Wang, and K.-T. Chao, *Phys. Rev. D* **84**, 114001 (2011), arXiv:1012.1030 [hep-ph].
- [101] B. Gong, L.-P. Wan, J.-X. Wang, and H.-F. Zhang, *Phys. Rev. Lett.* **110**, 042002 (2013), arXiv:1205.6682 [hep-ph].
- [102] M. Butenschoen and B. A. Kniehl, (2022), arXiv:2207.09346 [hep-ph].
- [103] G. T. Bodwin, K.-T. Chao, H. S. Chung, U.-R. Kim, J. Lee, and Y.-Q. Ma, *Phys. Rev. D* **93**, 034041 (2016), arXiv:1509.07904 [hep-ph].
- [104] F. Arleo, C.-J. Naïm, and S. Platchkov, *JHEP* **01**, 129 (2019), arXiv:1810.05120 [hep-ph].

- [105] C. Bourrely, W.-C. Chang, and J.-C. Peng, *Phys. Rev. D* **105**, 076018 (2022), [arXiv:2202.12547 \[hep-ph\]](#).
- [106] M. Aghasyan *et al.* (COMPASS), *Phys. Rev. Lett.* **119**, 112002 (2017), [arXiv:1704.00488 \[hep-ex\]](#).
- [107] B. Adams *et al.*, (2018), [arXiv:1808.00848 \[hep-ex\]](#).
- [108] A. C. Aguilar *et al.*, *Eur. Phys. J. A* **55**, 190 (2019), [arXiv:1907.08218 \[nucl-ex\]](#).
- [109] D. P. Anderle *et al.*, *Front. Phys. (Beijing)* **16**, 64701 (2021), [arXiv:2102.09222 \[nucl-ex\]](#).
- [110] J. M. M. Chávez, V. Bertone, F. De Soto Borrero, M. Defurne, C. Mezrag, H. Moutarde, J. Rodríguez-Quintero, and J. Segovia, *Phys. Rev. Lett.* **128**, 202501 (2022), [arXiv:2110.09462 \[hep-ph\]](#).

SUPPLEMENTAL MATERIALS

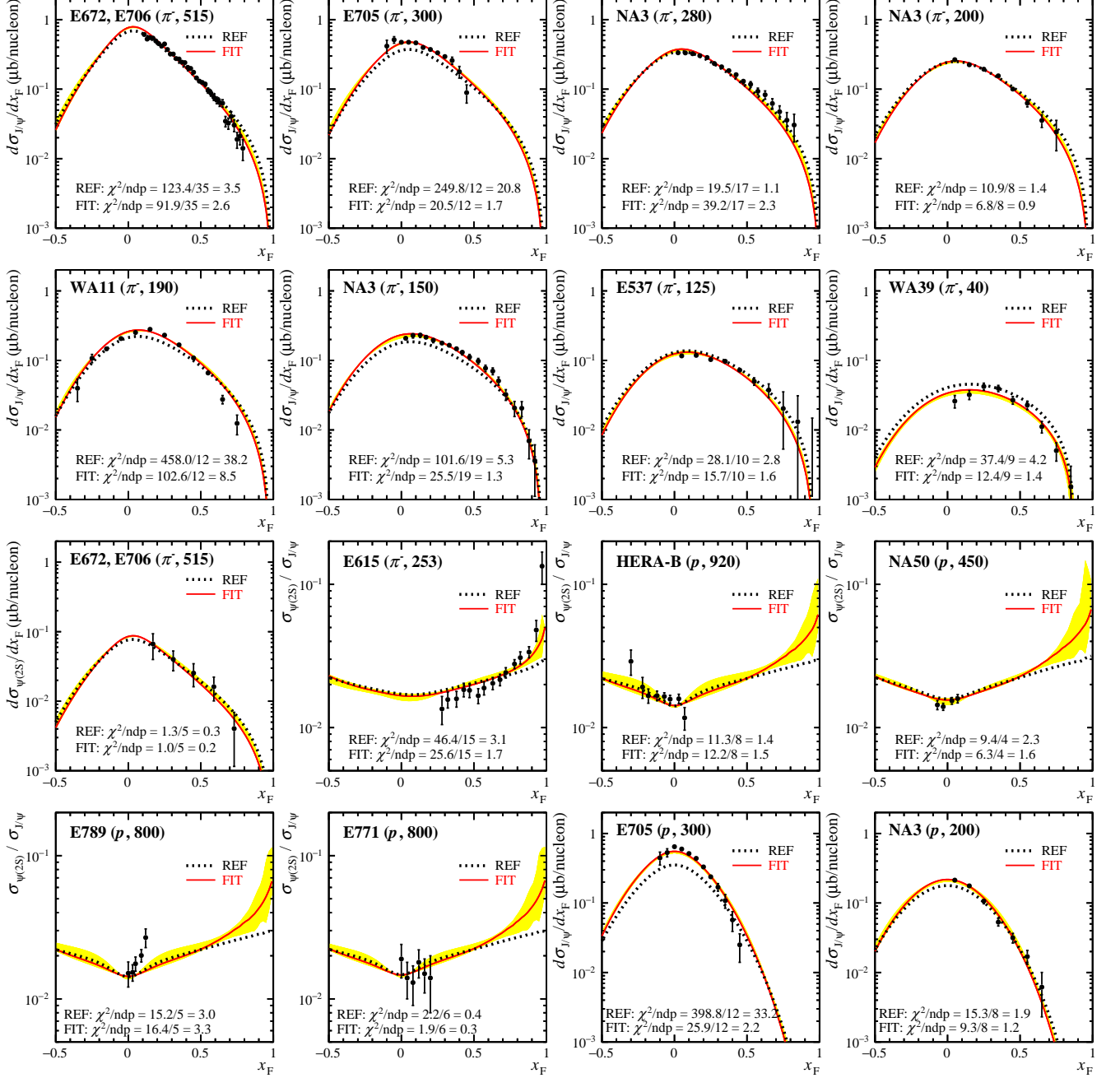


FIG. 1. The x_F -dependent cross sections for J/ψ and $\psi(2S)$ production and $R_{\psi}(x_F)$ ratios in $\pi^- N$ and pN interactions, following the order given in Table. II. The symbol and value in parenthesis denote the particle type and momentum of beam. The solid red and dotted black curves represent the NRQCD results of GRV pion PDFs from the fit described in the text (“FIT”) and from the calculation using the LDMEs obtained in Ref. [59] (“REF”), respectively. The values of χ^2 divided by the number of data point (ndp) for each dataset are also shown.

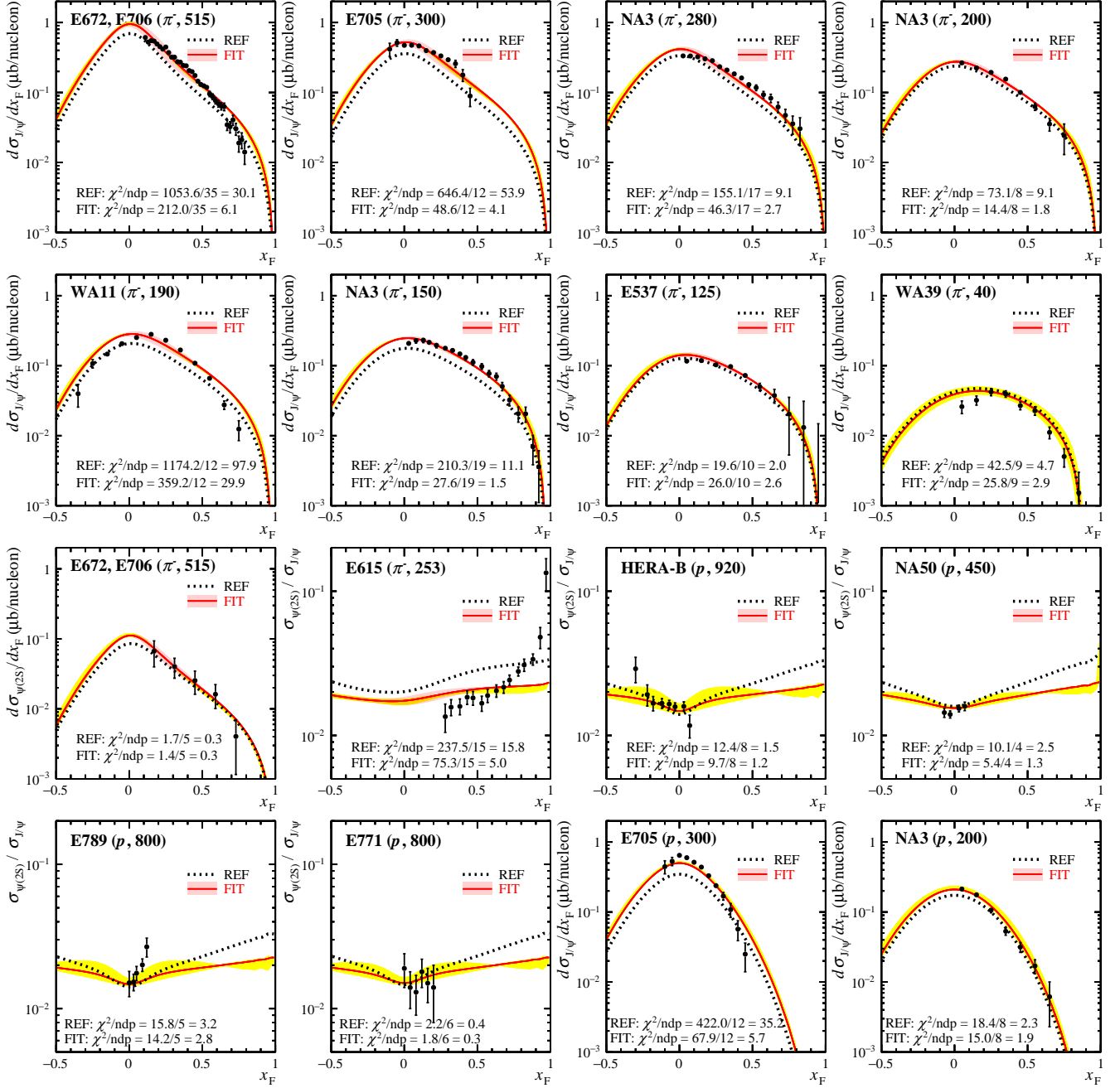


FIG. 2. The x_F -dependent cross sections for J/ψ and $\psi(2S)$ production and $R_\psi(x_F)$ ratios in $\pi^- N$ and pN interactions, following the order given in Table II. The symbol and value in parenthesis denote the particle type and momentum of beam. The solid red and dotted black curves represent the NRQCD results of JAM pion PDFs from the fit described in the text (“FIT”) and from the calculation using the LDMEs obtained in Ref. [59] (“REF”), respectively. The values of χ^2 divided by the number of data point (ndp) for each dataset are also shown. The yellow bands represent the cross section uncertainties associated with the scale and charm quark mass systematic variations.

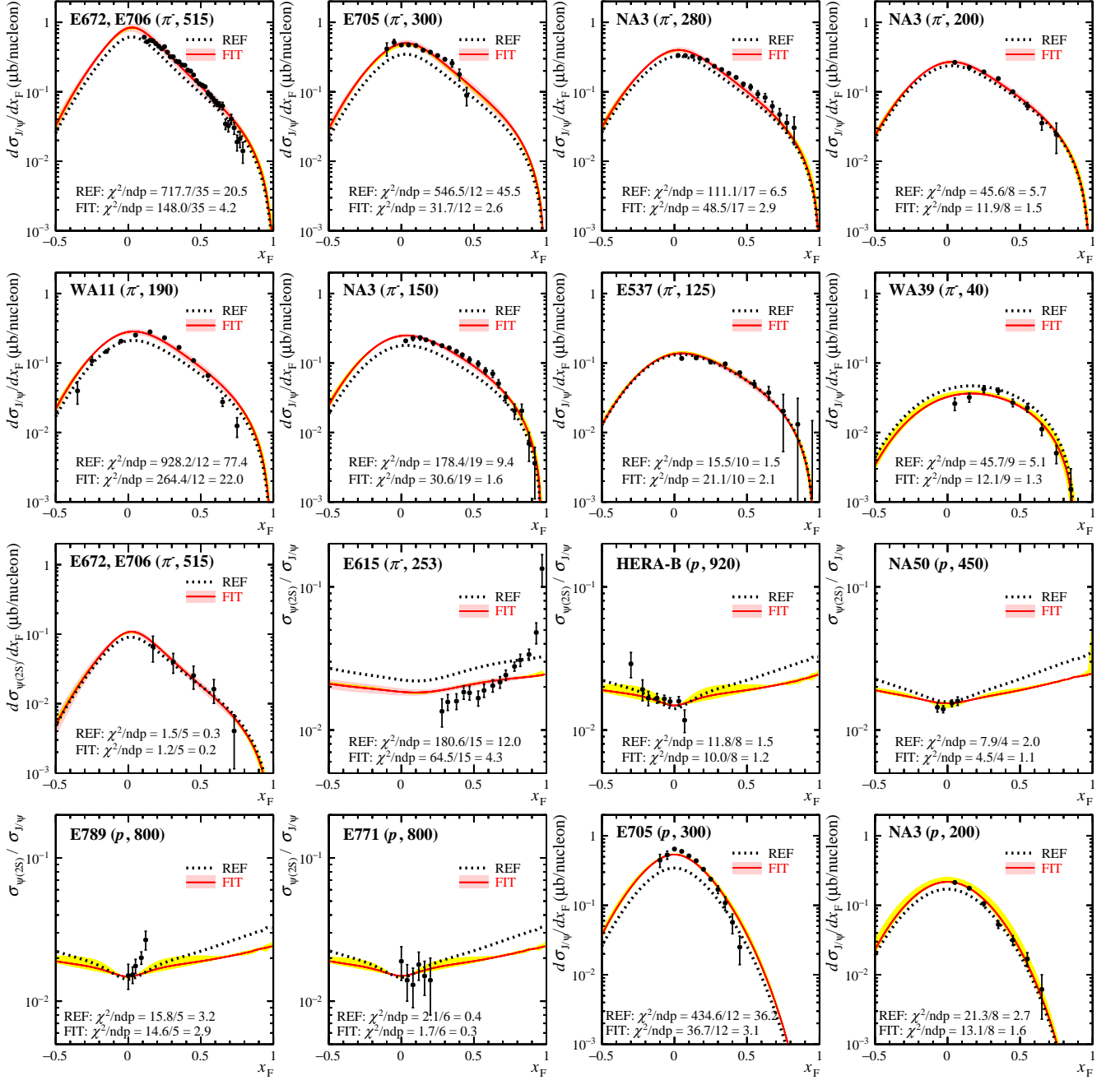


FIG. 3. The x_F -dependent cross sections for J/ψ and $\psi(2S)$ production and $R_\psi(x_F)$ ratios in π^-N and pN interactions, following the order given in Table. II. The symbol and value in parenthesis denote the particle type and momentum of beam. The solid red and dotted black curves represent the NRQCD results of xFitter pion PDFs from the fit described in the text ("FIT") and from the calculation using the LDMEs obtained in Ref. [59] ("REF"), respectively. The values of χ^2 divided by the number of data point (ndp) for each dataset are also shown. The yellow bands represent the cross section uncertainties associated with the scale and charm quark mass systematic variations.

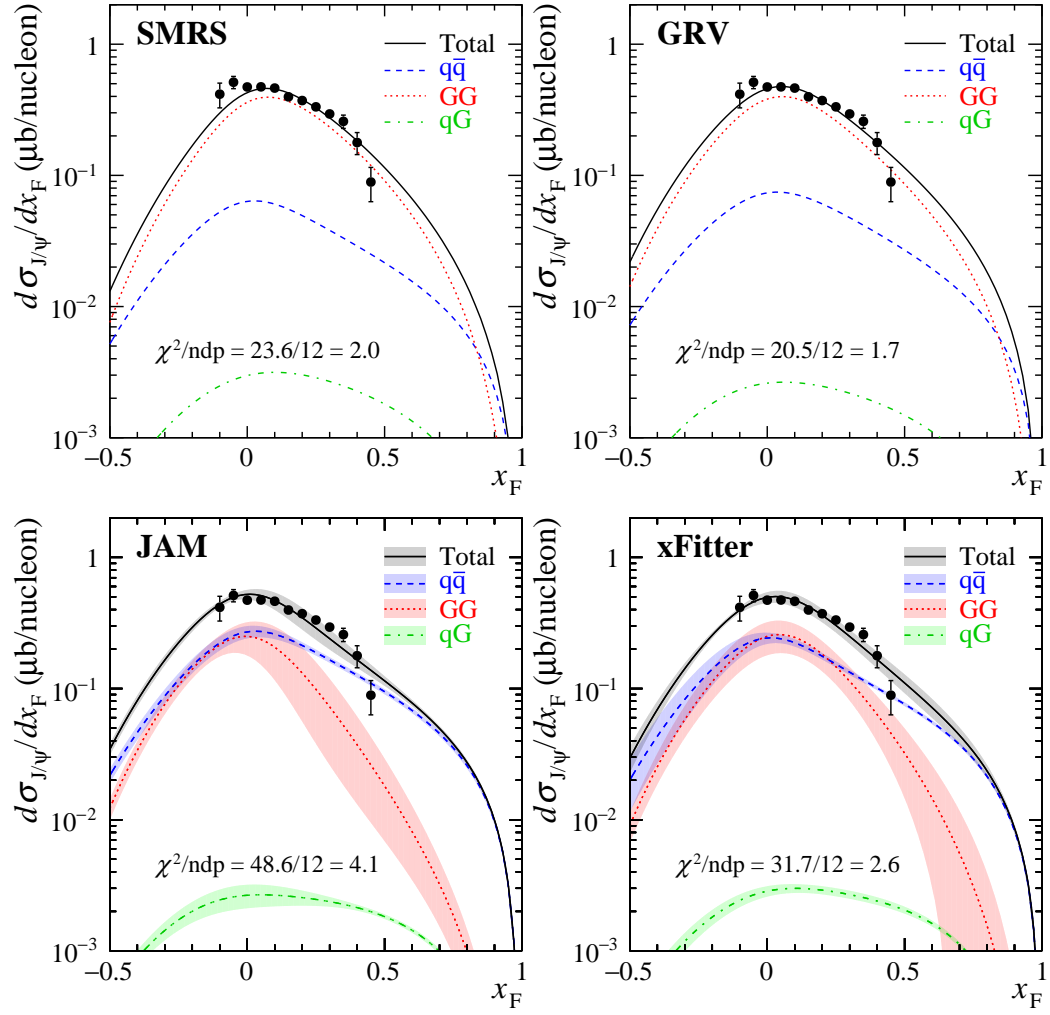


FIG. 4. Differential cross sections for J/ψ production with a 300-GeV/ c π^- beam from the E705 experiment [83]. The data are compared to the NRQCD fit results for the SMRS, GRV, xFitter, and JAM PDFs. The total cross sections and $q\bar{q}$, GG , and qG contributions are denoted as solid black, dashed blue, dotted red, and dot-dashed green lines, respectively. The uncertainty bands associated with JAM and xFitter PDFs are also shown.

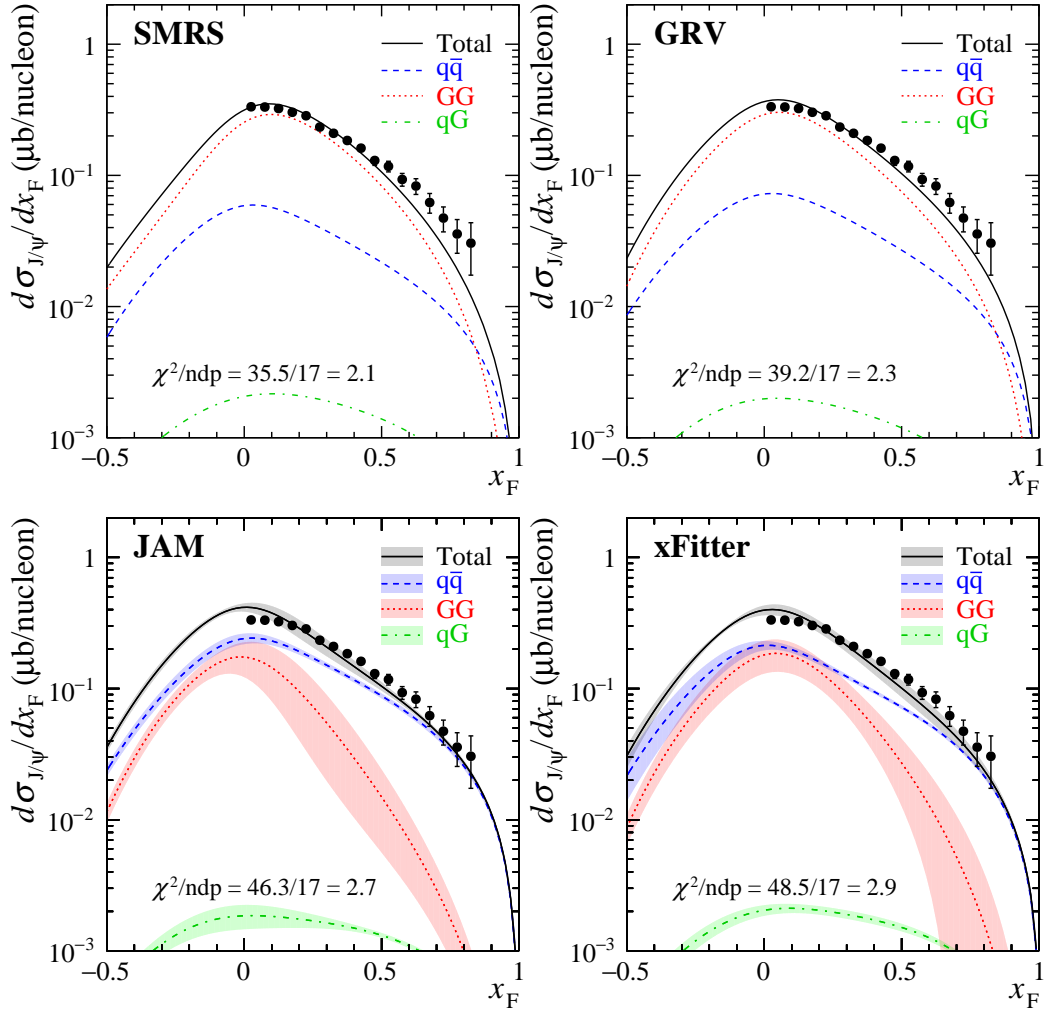


FIG. 5. Differential cross sections for J/ψ production with a 280-GeV/c π^- beam from the NA3 experiment [84]. The data are compared to the NRQCD fit results for the SMRS, GRV, xFitter, and JAM PDFs. The total cross sections and $q\bar{q}$, GG , and qG contributions are denoted as solid black, dashed blue, dotted red, and dot-dashed green lines, respectively. The uncertainty bands associated with JAM and xFitter PDFs are also shown.

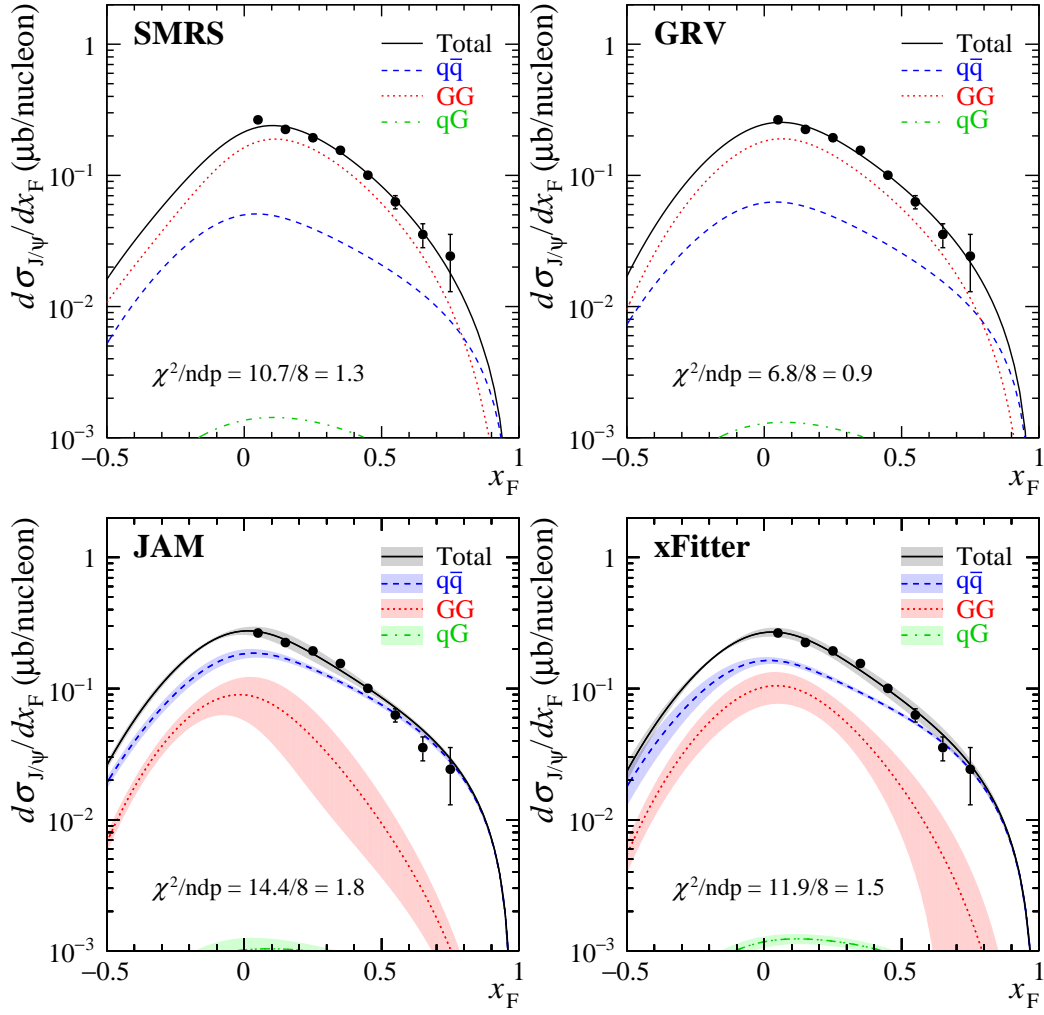


FIG. 6. Differential cross sections for J/ψ production with a 200-GeV/ c π^- beam from the NA3 experiment [84]. The data are compared to the NRQCD fit results for the SMRS, GRV, xFitter, and JAM PDFs. The total cross sections and $q\bar{q}$, GG , and qG contributions are denoted as solid black, dashed blue, dotted red, and dot-dashed green lines, respectively. The uncertainty bands associated with JAM and xFitter PDFs are also shown.

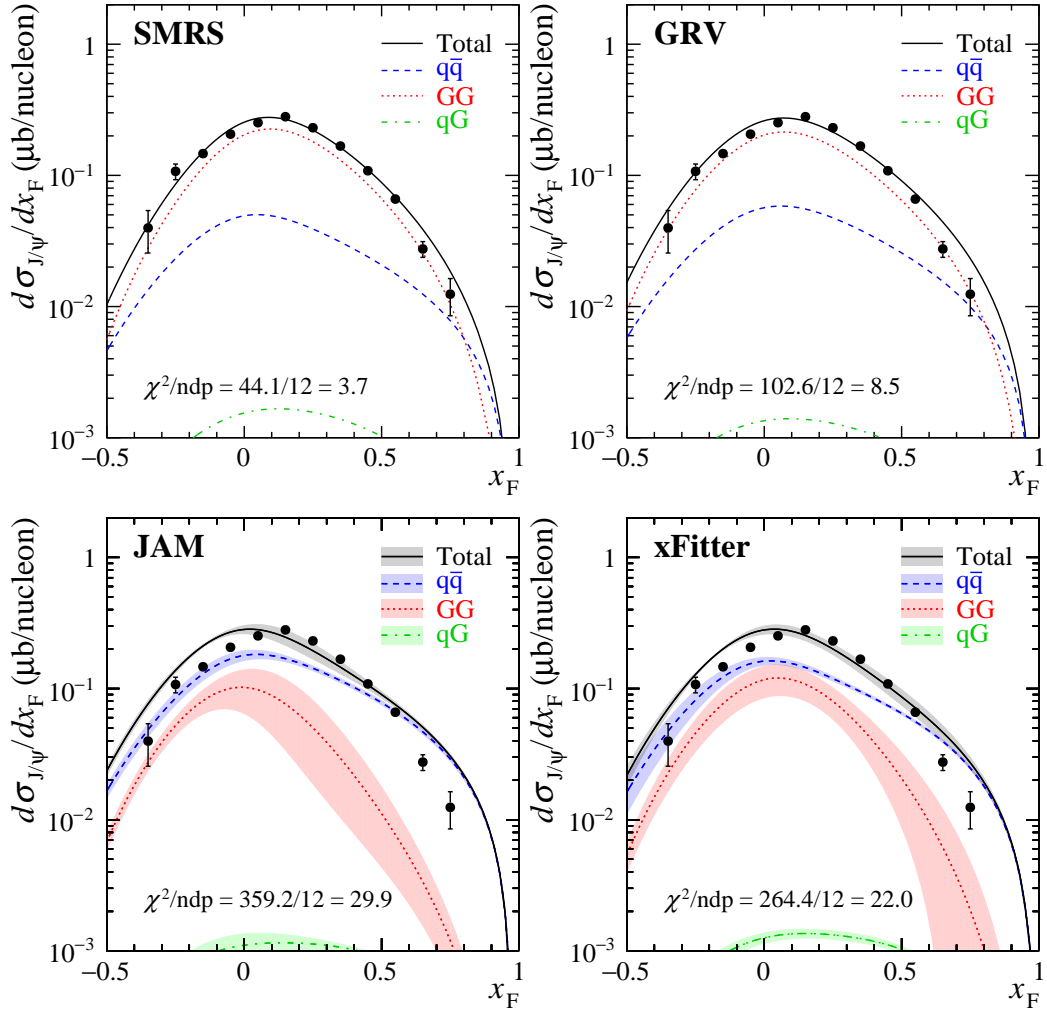


FIG. 7. Differential cross sections for J/ψ production with a 190-GeV/c π^- beam from the WA11 experiment [85]. The data are compared to the NRQCD fit results for the SMRS, GRV, xFitter, and JAM PDFs. The total cross sections and $q\bar{q}$, GG , and qG contributions are denoted as solid black, dashed blue, dotted red, and dot-dashed green lines, respectively. The uncertainty bands associated with JAM and xFitter PDFs are also shown.

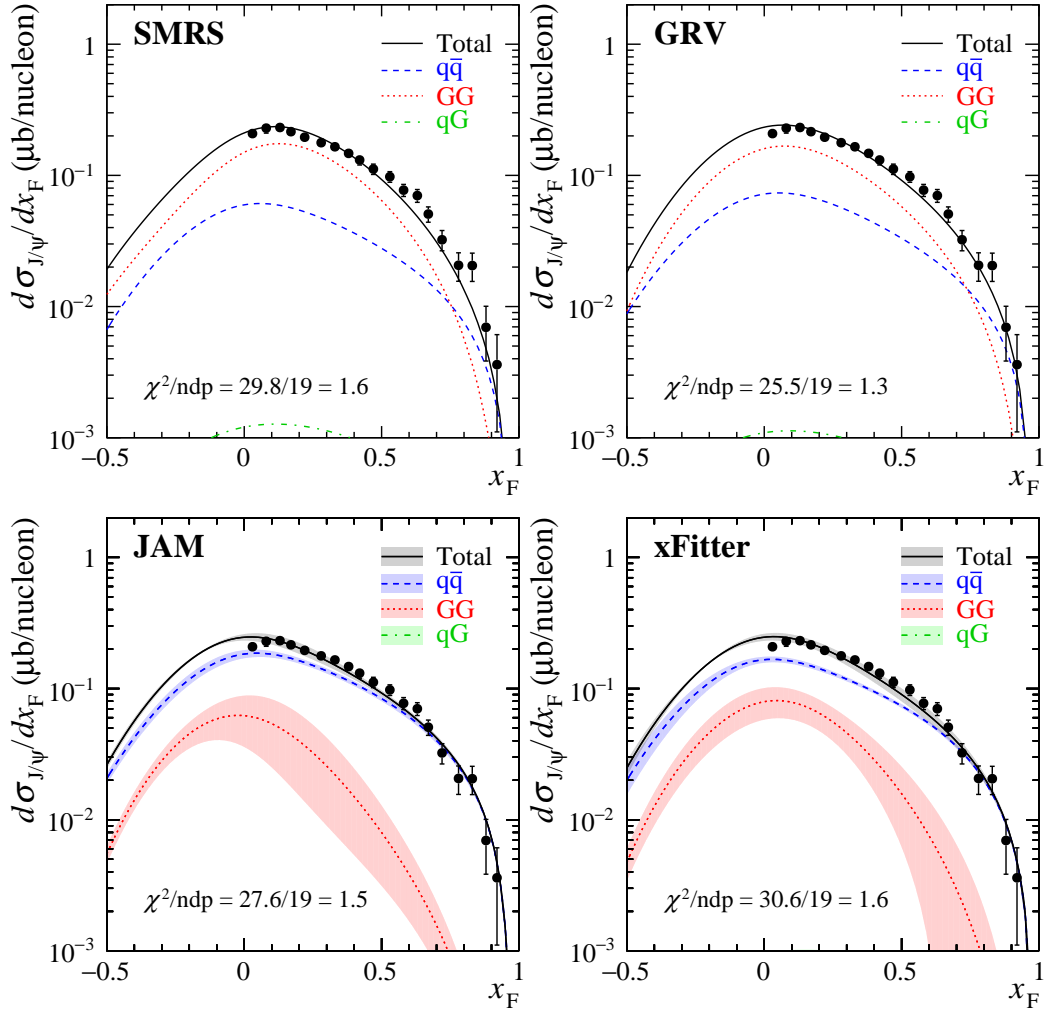


FIG. 8. Differential cross sections for J/ψ production with a 150-GeV/ c π^- beam from the NA3 experiment [84]. The data are compared to the NRQCD fit results for the SMRS, GRV, xFitter, and JAM PDFs. The total cross sections and $q\bar{q}$, GG , and qG contributions are denoted as solid black, dashed blue, dotted red, and dot-dashed green lines, respectively. The uncertainty bands associated with JAM and xFitter PDFs are also shown.

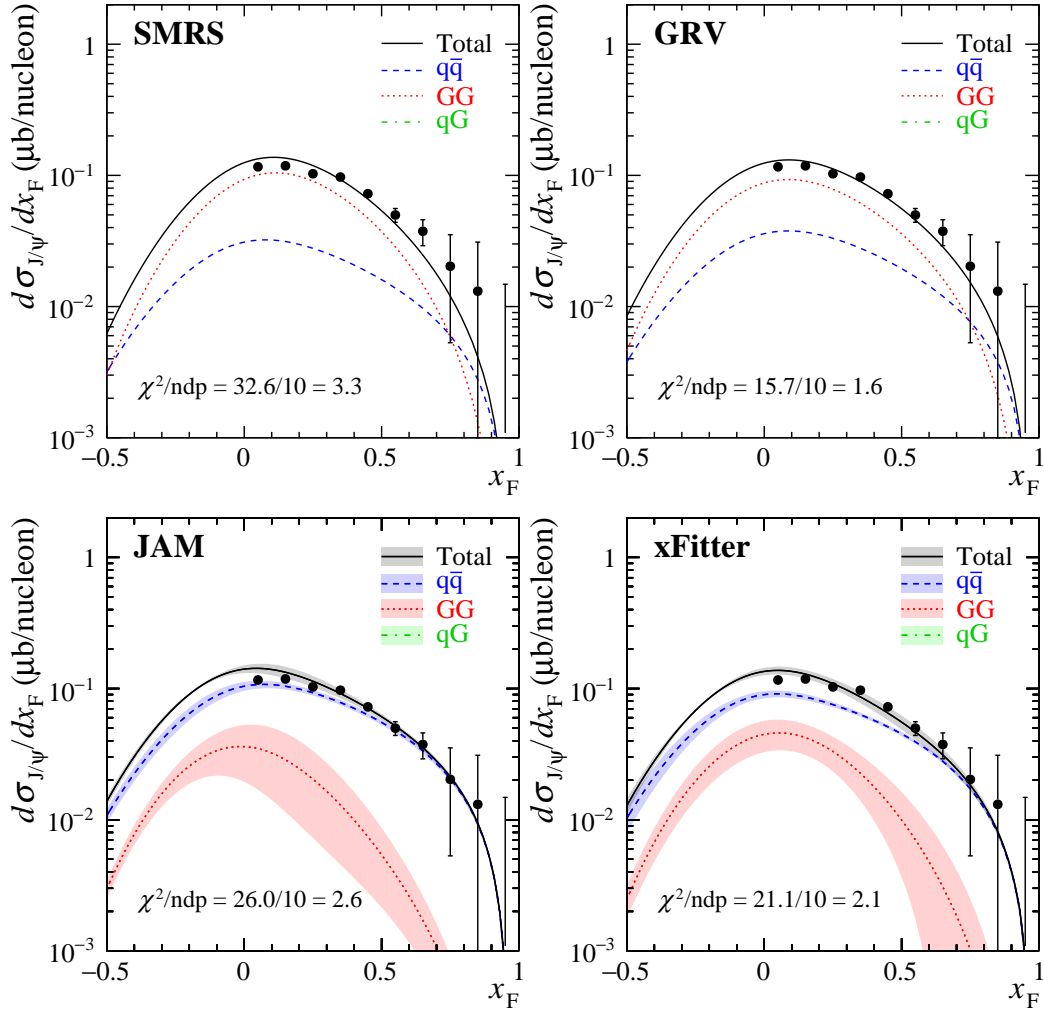


FIG. 9. Differential cross sections for J/ψ production with a 125-GeV/ c π^- beam from the E537 experiment [86]. The data are compared to the NRQCD fit results for the SMRS, GRV, xFitter, and JAM PDFs. The total cross sections and $q\bar{q}$, GG , and qG contributions are denoted as solid black, dashed blue, dotted red, and dot-dashed green lines, respectively. The uncertainty bands associated with JAM and xFitter PDFs are also shown.

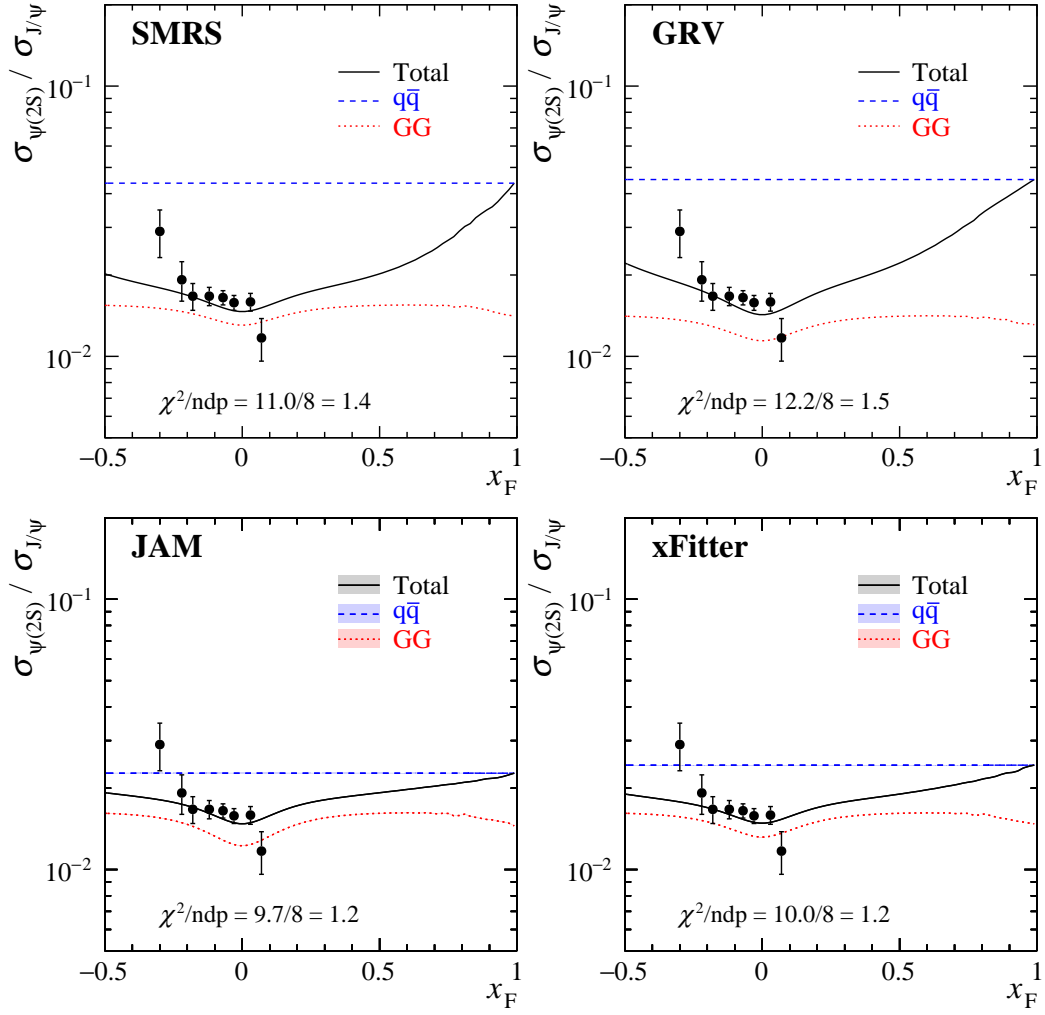


FIG. 10. The $\psi(2S)$ to J/ψ cross section ratios $R_\psi(x_F)$ for J/ψ and $\psi(2S)$ production with a 920-GeV/ c proton beam from the HERA-B experiment [78]. The data are compared to the NRQCD fit results for the SMRS, GRV, xFitter, and JAM PDFs. The ratios of total cross sections and individual $R_\psi^{q\bar{q}}(x_F)$ and $R_\psi^{GG}(x_F)$ contributions are denoted as solid black, dashed blue, and dotted red lines, respectively.

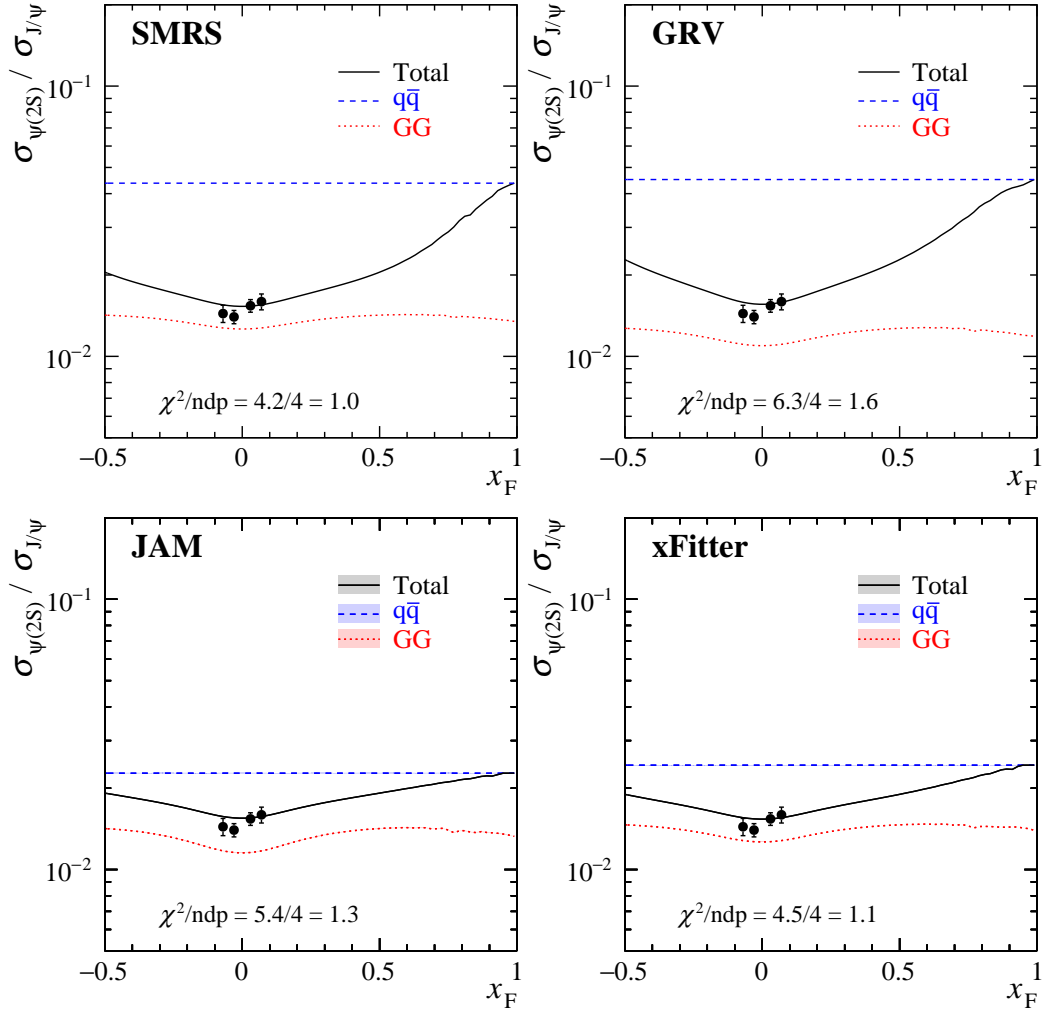


FIG. 11. The $\psi(2S)$ to J/ψ cross section ratios $R_\psi(x_F)$ for J/ψ and $\psi(2S)$ production with a 450-GeV/c proton beam from the NA50 experiment [89]. The data are compared to the NRQCD fit results for the SMRS, GRV, xFitter, and JAM PDFs. The ratios of total cross sections and individual $R_\psi^{q\bar{q}}(x_F)$ and $R_\psi^{GG}(x_F)$ contributions are denoted as solid black, dashed blue, and dotted red lines, respectively.

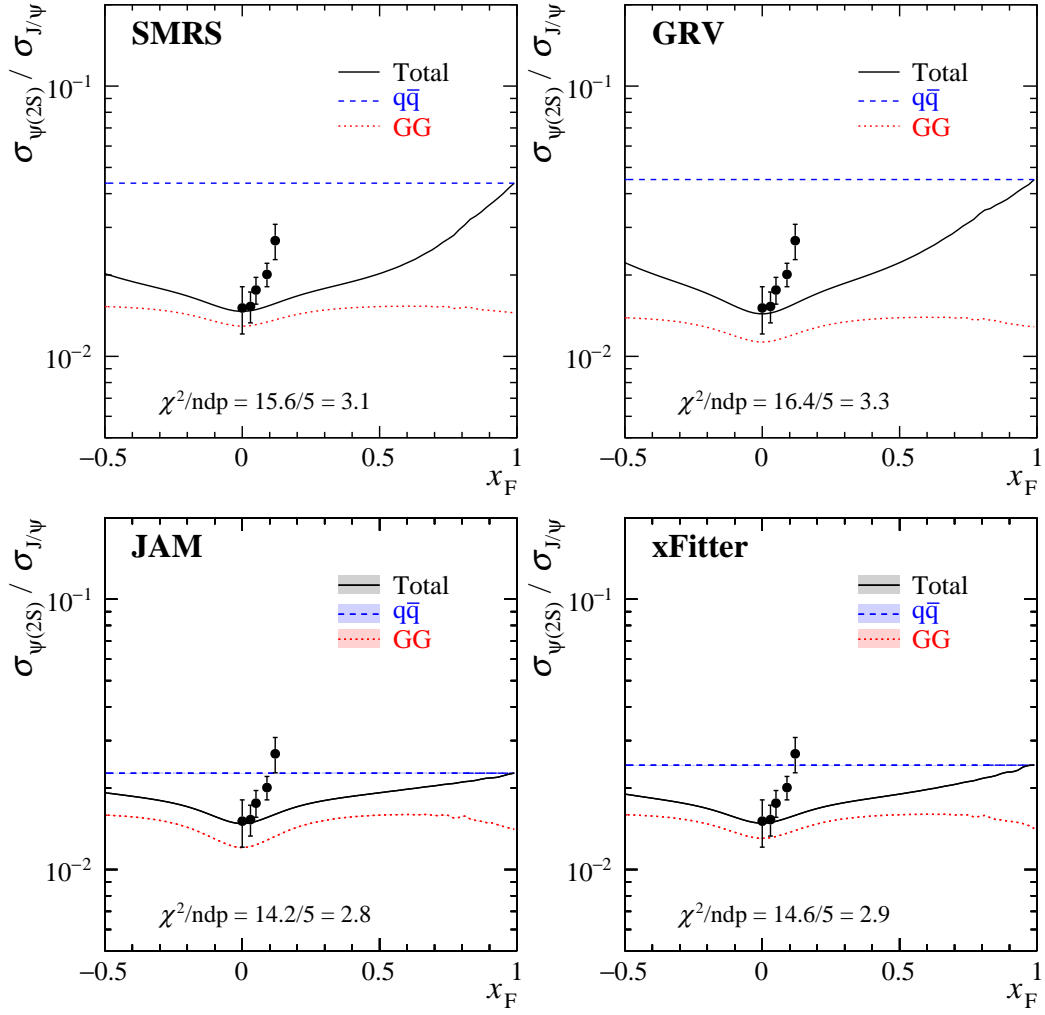


FIG. 12. The $\psi(2S)$ to J/ψ cross section ratios $R_\psi(x_F)$ for J/ψ and $\psi(2S)$ production with a 450-GeV/c proton beam from the NA50 experiment [89]. The data are compared to the NRQCD fit results for the SMRS, GRV, xFitter, and JAM PDFs. The ratios of total cross sections and individual $R_\psi^{q\bar{q}}(x_F)$ and $R_\psi^{GG}(x_F)$ contributions are denoted as solid black, dashed blue, and dotted red lines, respectively.

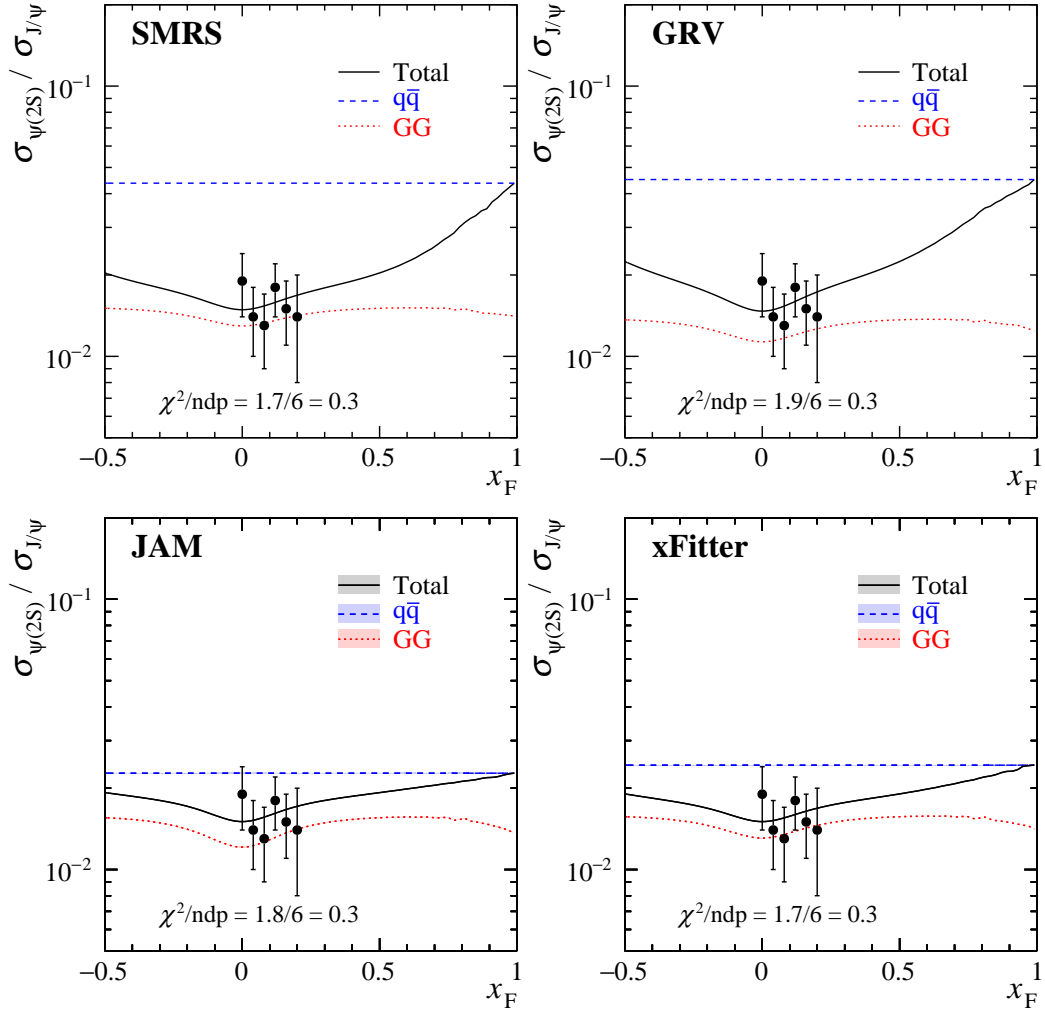


FIG. 13. The $\psi(2S)$ to J/ψ cross section ratios $R_\psi(x_F)$ for J/ψ and $\psi(2S)$ production with a 800-GeV/c proton beam from the E771 experiment [91]. The ratios of total cross sections and individual $R_\psi^{q\bar{q}}(x_F)$ and $R_\psi^{GG}(x_F)$ contributions are denoted as solid black, dashed blue, and dotted red lines, respectively.

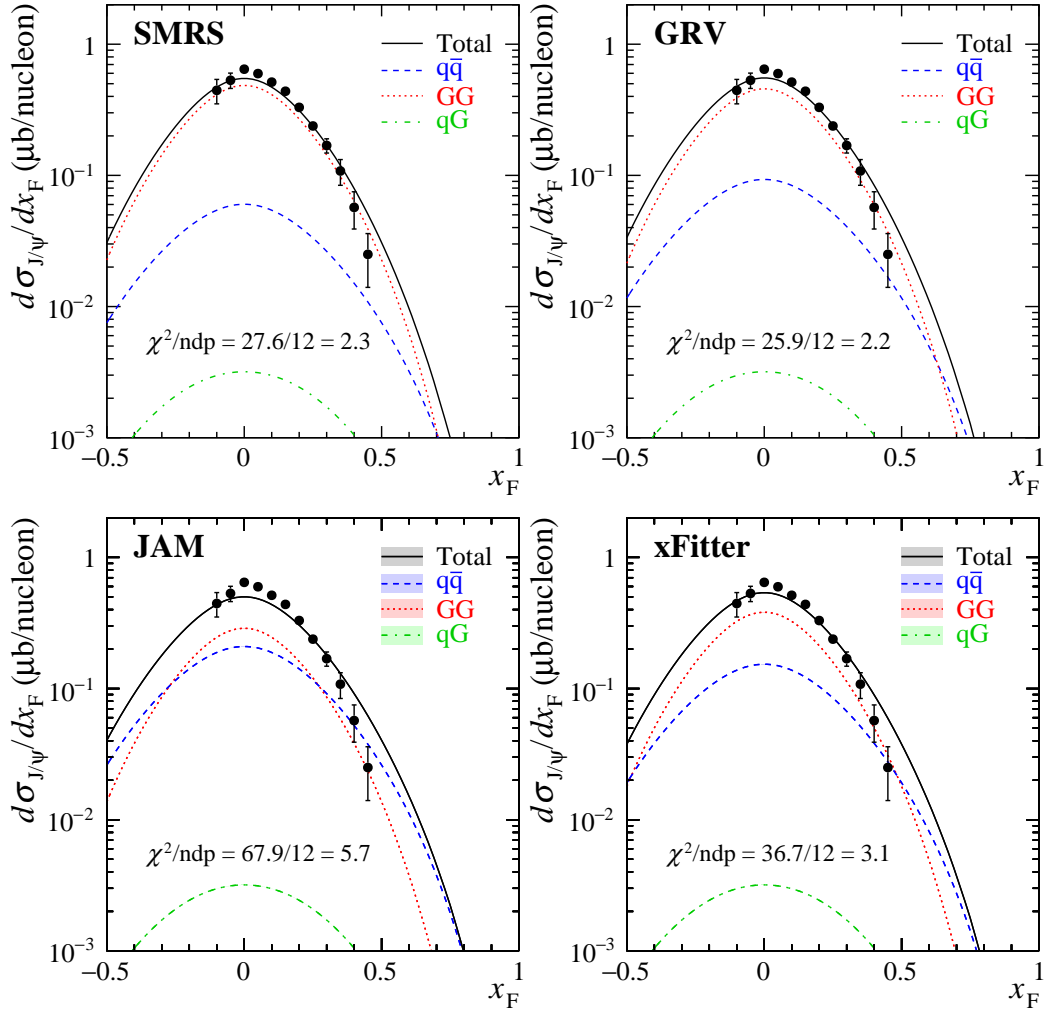


FIG. 14. Differential cross sections for J/ψ production with a 300-GeV/c proton beam from the E705 experiment [83]. The data are compared to the NRQCD fit results of LDMEs for the SMRS, GRV, xFitter, and JAM PDFs. The total cross sections and $q\bar{q}$, GG , and qG contributions are denoted as solid black, dashed blue, dotted red, and dot-dashed green lines, respectively.

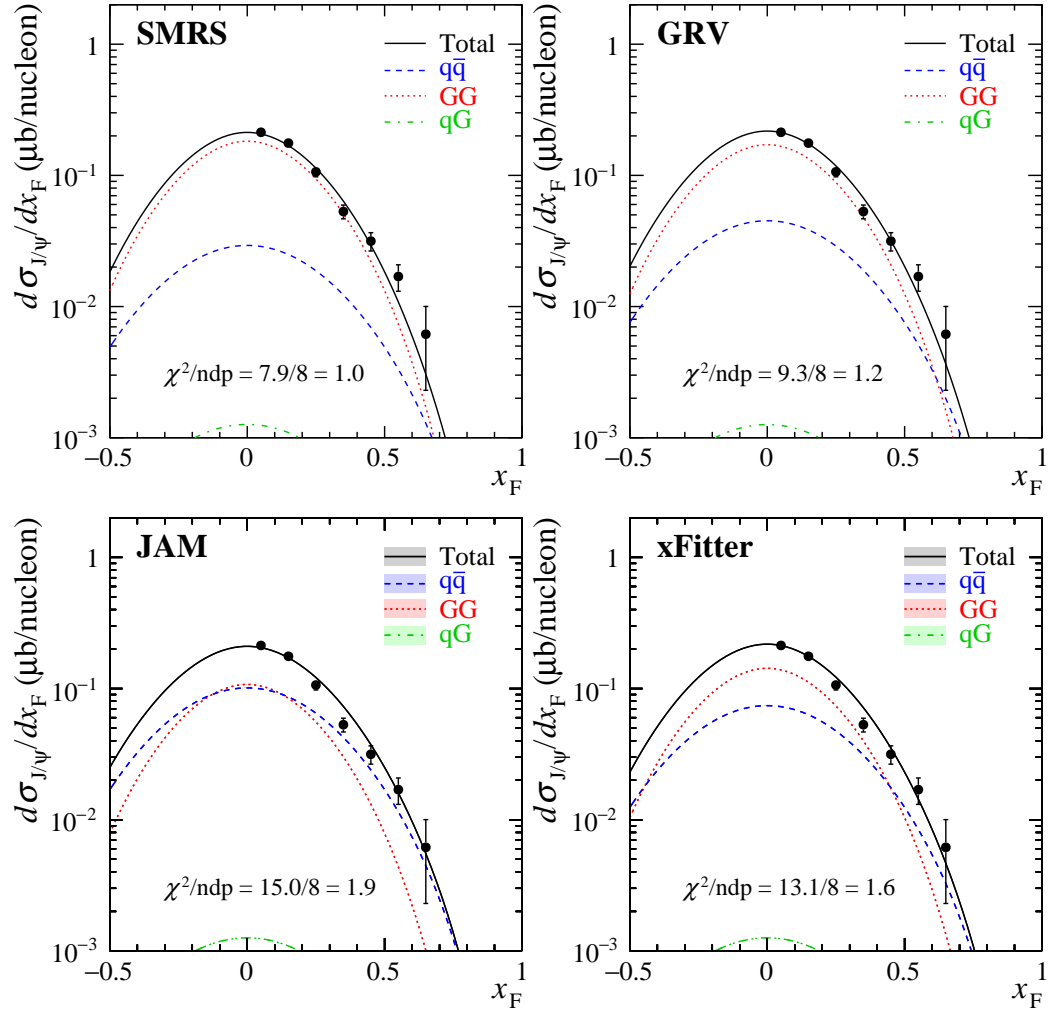


FIG. 15. Differential cross sections for J/ψ production with a 200-GeV/c proton beam from the NA3 experiment [84]. The data are compared to the NRQCD fit results of LDMEs for the SMRS, GRV, xFitter, and JAM PDFs. The total cross sections and $q\bar{q}$, GG , and qG contributions are denoted as solid black, dashed blue, dotted red, and dot-dashed green lines, respectively.

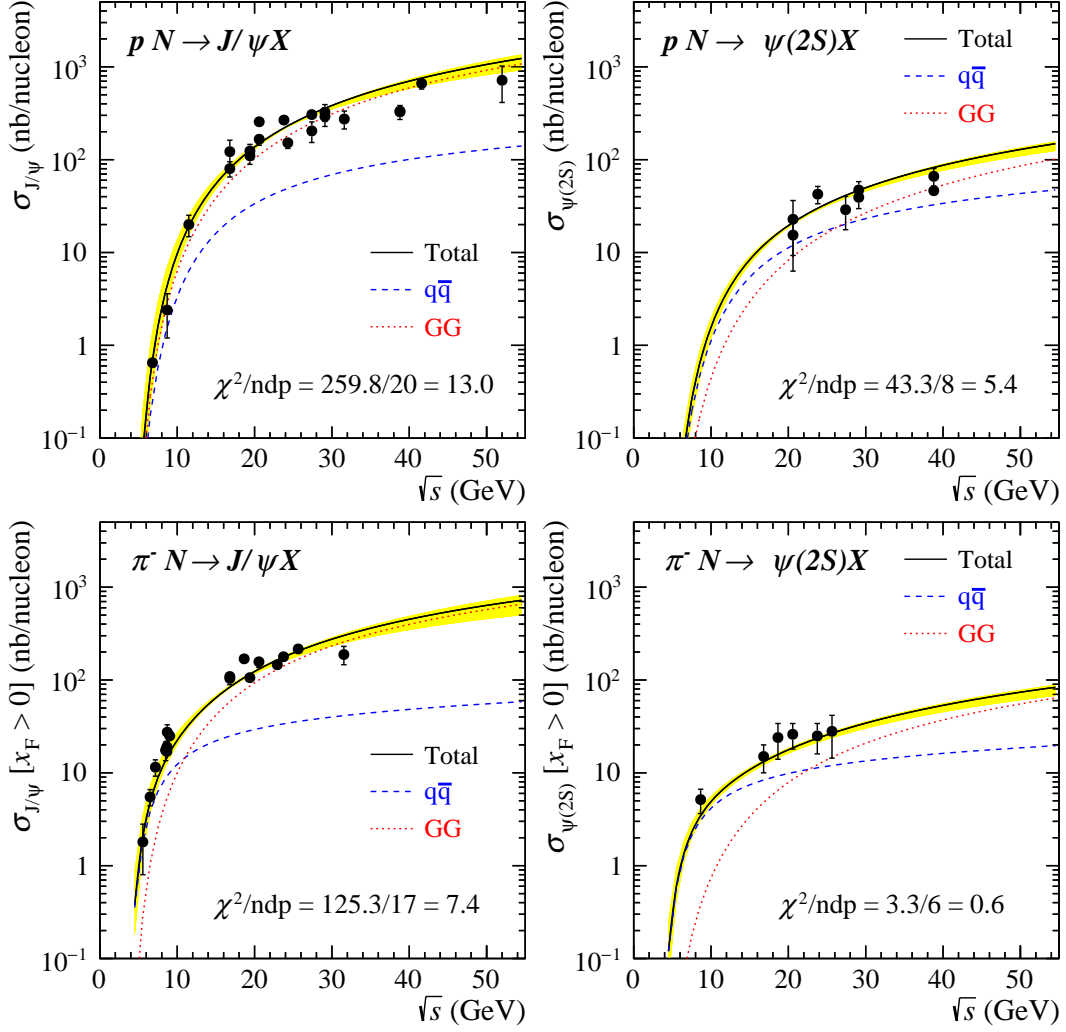


FIG. 16. Integrated charmonium cross sections in pN and $\pi^- N$ collisions. The data for J/ψ and $\psi(2S)$ production are compared to the fit made using the GRV pion PDFs. The total cross section and its $q\bar{q}$ and GG contributions are denoted as solid black, dashed blue and dotted red lines, respectively. The yellow bands represent the cross section uncertainties associated with the scale and charm quark mass systematic variations.

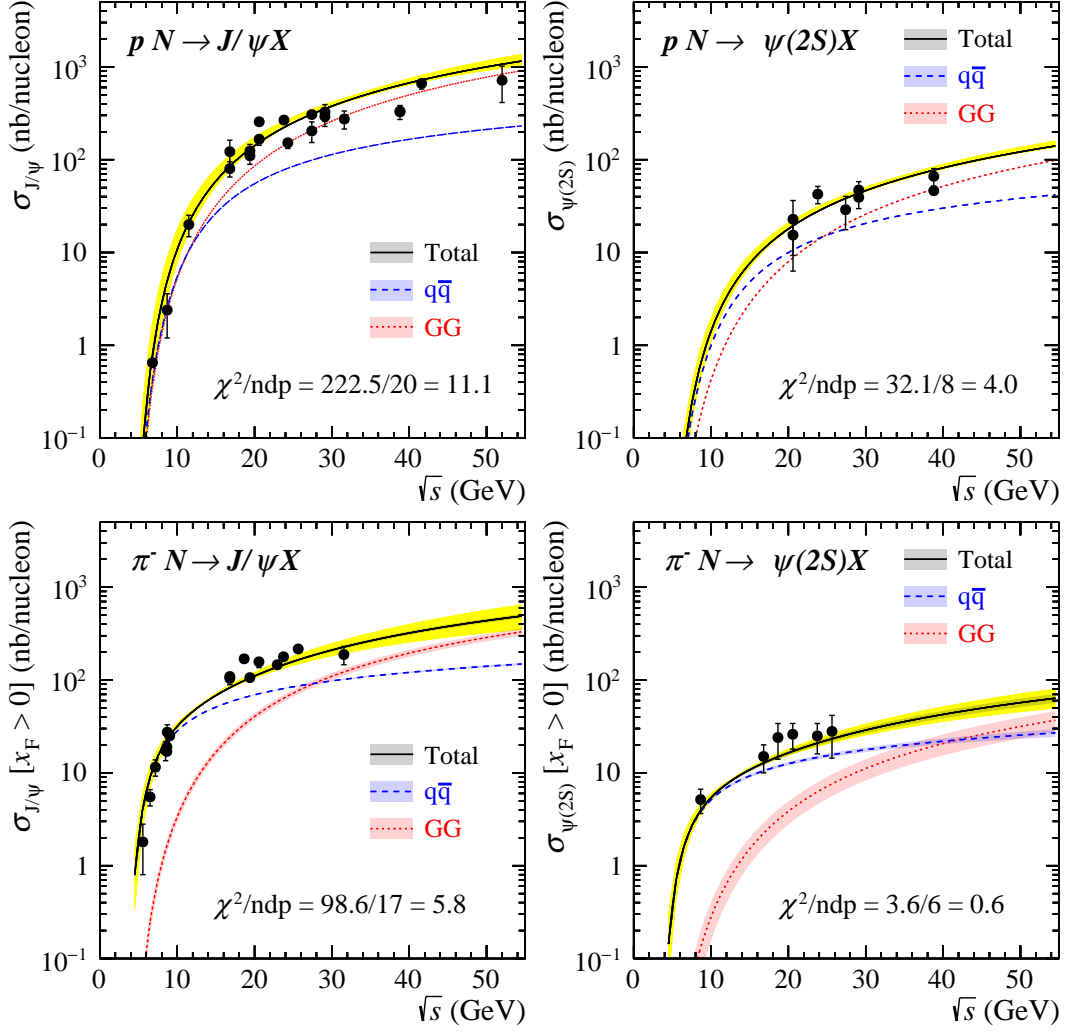


FIG. 17. Integrated charmonium cross sections in pN and $\pi^- N$ collisions. The data for J/ψ and $\psi(2S)$ production are compared to the fit made using the JAM pion PDFs. The total cross section and its $q\bar{q}$ and GG contributions are denoted as solid black, dashed blue and dotted red lines, respectively. The uncertainty bands associated with JAM PDFs are also shown. The yellow bands represent the cross section uncertainties associated with the scale and charm quark mass systematic variations.

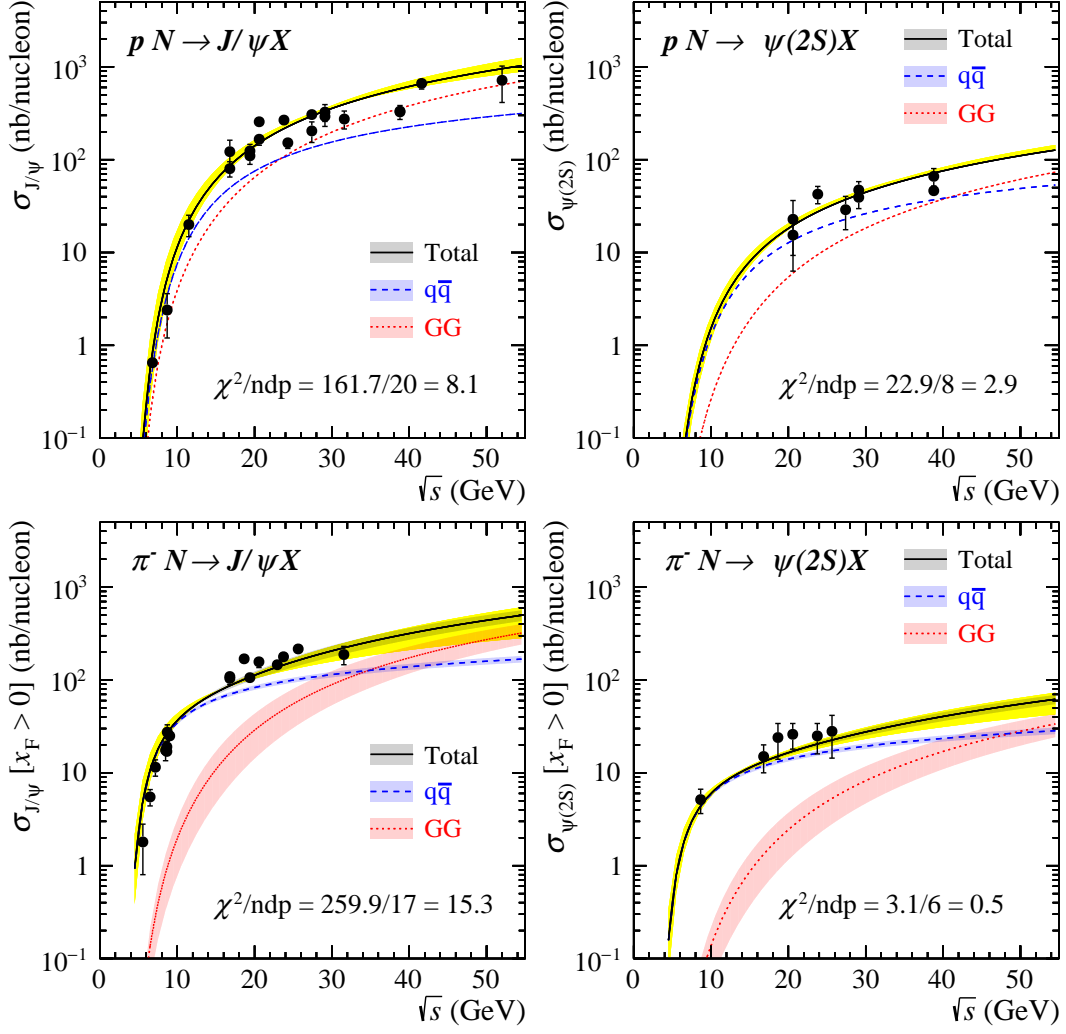


FIG. 18. Integrated charmonium cross sections in pN and $\pi^- N$ collisions. The data for J/ψ and $\psi(2S)$ production are compared to the fit made using the xFitter pion PDFs. The total cross section and its $q\bar{q}$ and GG contributions are denoted as solid black, dashed blue and dotted red lines, respectively. The uncertainty bands associated with xFitter PDFs are also shown. The yellow bands represent the cross section uncertainties associated with the scale and charm quark mass systematic variations.

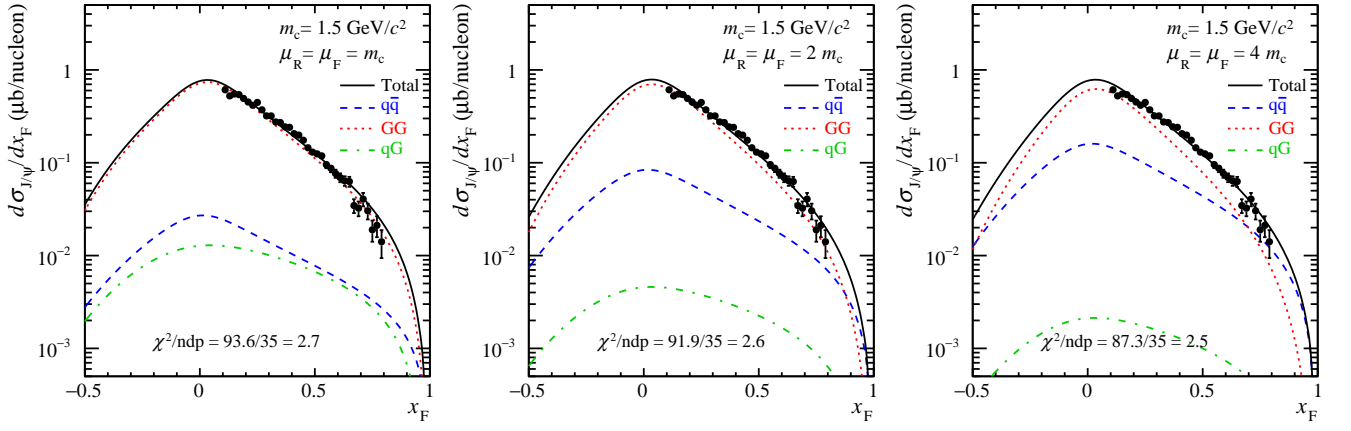


FIG. 19. The NRQCD results with variation of charm quark mass m_c and renormalization scale μ_R , compared with the $d\sigma/dx_F$ data of J/ψ production off the beryllium target with a 515-GeV/c π^- beam from the E672/E706 experiment [82]. The pion PDFs used for the calculation is GRV. The total cross sections and $q\bar{q}$, GG , and qG contributions are denoted as solid black, dashed blue, dotted red and dot-dashed green lines, respectively. The charm quark mass m_c , factorization scale μ_F , and renormalization scale μ_R used for the NRQCD calculation as well as the fit χ^2/ndf are displayed in each plot.

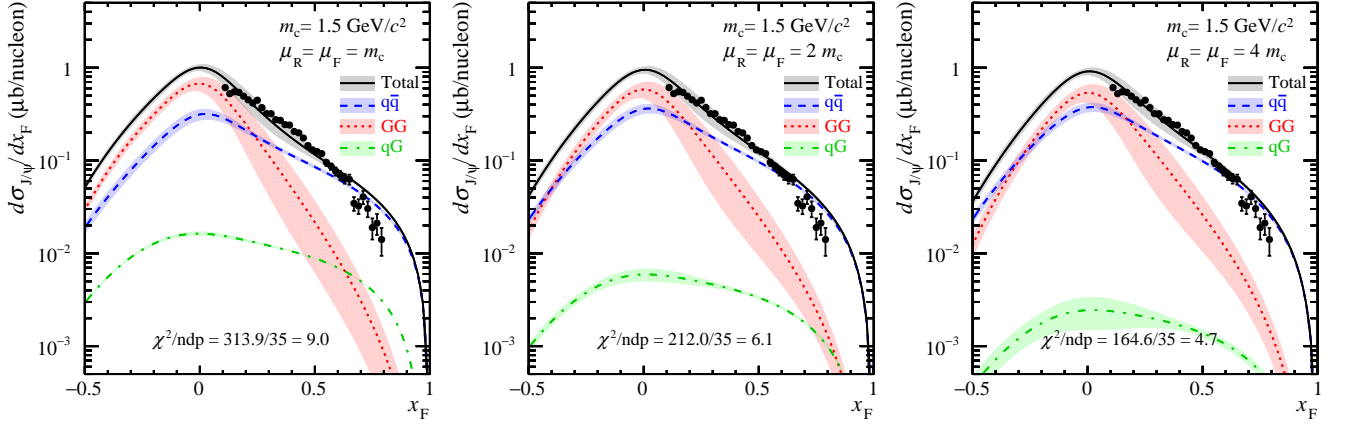


FIG. 20. Same as Fig. 19 but with the input of JAM pion PDFs.

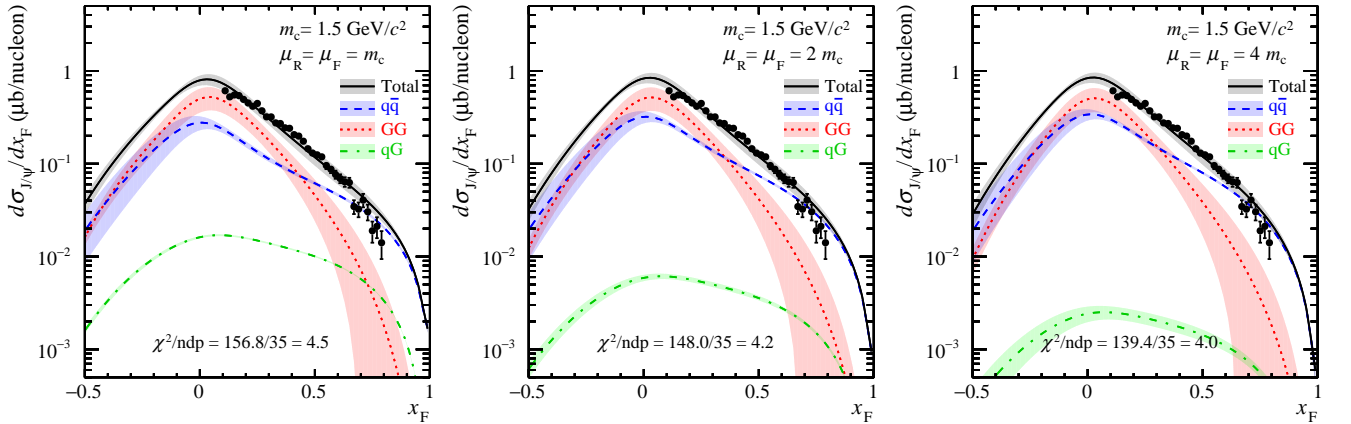


FIG. 21. Same as Fig. 19 but with the input of xFitter pion PDFs.

m_c (GeV/ c^2)	SMRS					
	1.5			1.4	1.5	1.6
μ/m_c	1	2	4	2		
χ^2_{total}/ndf	2.5	1.9	2.7	2.0	1.9	2.0
$\chi^2/ndp _{x_F}^{\pi^-}$	2.3	1.8	2.4	2.0	1.8	1.7
$\chi^2/ndp _{x_F}^p$	2.3	1.6	3.0	1.4	1.6	2.1
$\chi^2/ndp _{\sqrt{s}}^{\pi^-}$	4.6	8.7	4.3	6.7	8.7	10.7
$\chi^2/ndp _{\sqrt{s}}^p$	5.0	8.1	8.7	6.6	8.1	9.4
$\langle \mathcal{O}_8^{J/\psi} [{}^3S_1] \rangle$	1.6E-02	2.6E-02	9.7E-02	1.2E-02	2.6E-02	5.2E-02
	$\pm 1.6E-03$	$\pm 2.3E-03$	$\pm 5.7E-03$	$\pm 1.6E-03$	$\pm 2.3E-03$	$\pm 4.6E-03$
$\Delta_8^{J/\psi}$	1.3E-02	5.6E-02	9.3E-02	2.0E-02	5.6E-02	1.1E-01
$//'$	$\pm 7.9E-04$	$\pm 1.6E-03$	$\pm 2.4E-03$	$\pm 9.8E-04$	$\pm 1.6E-03$	$\pm 2.3E-03$
$\langle \mathcal{O}_8^{\psi(2S)} [{}^3S_1] \rangle$	7.7E-03	1.3E-02	2.9E-02	8.0E-03	1.3E-02	2.2E-02
	$\pm 4.0E-04$	$\pm 8.6E-04$	$\pm 1.4E-03$	$\pm 4.8E-04$	$\pm 8.6E-04$	$\pm 1.5E-03$
$\Delta_8^{\psi(2S)}$	2.5E-04	5.7E-03	9.1E-03	1.7E-03	5.7E-03	1.1E-02
	$\pm 1.9E-04$	$\pm 2.9E-04$	$\pm 5.4E-04$	$\pm 1.5E-04$	$\pm 2.9E-04$	$\pm 5.8E-04$

TABLE V. The reduced χ^2/ndf of values for the whole data sets and the χ^2 divided by the number of data point (ndf) for the pion-induced and proton-induced datasets with the systematic variation of charm quark mass m_c of 1.4, 1.5 and 1.6 GeV/ c^2 , and $\mu = \mu_R = \mu_F$ at 1.0, 2.0, and 4.0 m_c in NRQCD calculations and the corresponding input or best-fit LDMEs for SMRS pion PDFs. All LDMEs are in units of GeV³.

m_c (GeV/ c^2)	GRV					
	1.5			1.4	1.5	1.6
μ/m_c	1	2	4	2		
χ^2_{total}/ndf	2.4	2.4	2.7	2.7	2.4	2.3
$\chi^2/ndp _{x_F}^{\pi^-}$	2.3	2.4	2.6	2.7	2.4	2.1
$\chi^2/ndp _{x_F}^p$	2.0	1.7	2.1	1.9	1.7	2.2
$\chi^2/ndp _{\sqrt{s}}^{\pi^-}$	8.4	5.6	2.8	2.1	5.6	8.7
$\chi^2/ndp _{\sqrt{s}}^p$	5.5	8.1	9.8	5.8	8.1	9.4
$\langle \mathcal{O}_8^{J/\psi} [{}^3S_1] \rangle$	1.5E-04	4.3E-02	1.4E-01	3.5E-02	4.3E-02	7.3E-02
	$\pm 1.3E-04$	$\pm 3.8E-03$	$\pm 8.4E-03$	$\pm 5.5E-05$	$\pm 3.8E-03$	$\pm 3.9E-03$
$\Delta_8^{J/\psi}$	1.9E-02	5.2E-02	8.8E-02	1.3E-02	5.2E-02	1.1E-01
$//'$	$\pm 1.4E-04$	$\pm 1.7E-03$	$\pm 2.8E-03$	$\pm 2.2E-05$	$\pm 1.7E-03$	$\pm 1.7E-03$
$\langle \mathcal{O}_8^{\psi(2S)} [{}^3S_1] \rangle$	8.4E-03	2.1E-02	4.2E-02	1.5E-02	2.1E-02	3.3E-02
	$\pm 5.8E-04$	$\pm 1.3E-03$	$\pm 3.1E-03$	$\pm 3.2E-05$	$\pm 1.3E-03$	$\pm 1.5E-03$
$\Delta_8^{\psi(2S)}$	5.2E-04	4.2E-03	7.2E-03	1.0E-04	4.2E-03	9.3E-03
	$\pm 2.5E-04$	$\pm 2.9E-04$	$\pm 8.3E-04$	$\pm 7.8E-05$	$\pm 2.9E-04$	$\pm 3.7E-04$

TABLE VI. The reduced χ^2/ndf of values for the whole data sets and the χ^2 divided by the number of data point (ndf) for the pion-induced and proton-induced datasets with the systematic variation of charm quark mass m_c of 1.4, 1.5 and 1.6 GeV/ c^2 , and $\mu = \mu_R = \mu_F$ at 1.0, 2.0, and 4.0 m_c in NRQCD calculations and the corresponding input or best-fit LDMEs for GRV pion PDFs. All LDMEs are in units of GeV³.

m_c (GeV/ c^2)	JAM					
	1.5			1.4	1.5	1.6
μ/m_c	1	2	4	2		
χ^2_{total}/ndf	8.2	5.6	4.7	6.3	5.6	5.0
$\chi^2/ndp _{x_F}^{\pi^-}$	8.7	5.9	4.9	6.9	5.9	5.2
$\chi^2/ndp _{x_F}^p$	4.0	2.7	2.5	2.5	2.7	2.7
$\chi^2/ndp _{\sqrt{s}}^{\pi^-}$	31.3	11.4	4.9	31.4	11.4	9.4
$\chi^2/ndp _{\sqrt{s}}^p$	6.8	5.1	7.5	5.4	5.1	7.7
$\langle \mathcal{O}_8^{J/\psi} [^3S_1] \rangle$	6.0E-02	1.2E-01	2.1E-01	7.2E-02	1.2E-01	1.9E-01
	$\pm 1.2E-03$	$\pm 2.1E-03$	$\pm 4.0E-03$	$\pm 1.7E-03$	$\pm 2.1E-03$	$\pm 4.9E-01$
$\Delta_8^{J/\psi}$	3.5E-03	2.4E-02	6.2E-02	1.9E-03	2.4E-02	6.8E-02
$//'$	$\pm 6.9E-04$	$\pm 1.6E-03$	$\pm 2.6E-03$	$\pm 8.0E-04$	$\pm 1.6E-03$	$\pm 3.3E+00$
$\langle \mathcal{O}_8^{\psi(2S)} [^3S_1] \rangle$	1.1E-02	2.4E-02	4.0E-02	1.4E-02	2.4E-02	3.7E-02
	$\pm 3.6E-04$	$\pm 8.5E-04$	$\pm 1.5E-03$	$\pm 4.2E-04$	$\pm 8.5E-04$	$\pm 4.4E-01$
$\Delta_8^{\psi(2S)}$	1.9E-09	2.1E-03	5.9E-03	3.1E-08	2.1E-03	6.7E-03
	$\pm 1.1E-05$	$\pm 3.2E-04$	$\pm 5.4E-04$	$\pm 2.9E-05$	$\pm 3.2E-04$	$\pm 4.3E-01$

TABLE VII. The reduced χ^2/ndf of values for the whole data sets and the χ^2 divided by the number of data point (ndf) for the pion-induced and proton-induced datasets with the systematic variation of charm quark mass m_c of 1.4, 1.5 and 1.6 GeV/ c^2 , and $\mu = \mu_R = \mu_F$ at 1.0, 2.0, and 4.0 m_c in NRQCD calculations and the corresponding input or best-fit LDMEs for JAM pion PDFs. All LDMEs are in units of GeV³.

m_c (GeV/ c^2)	xFitter					
	1.5			1.4	1.5	1.6
μ/m_c	1	2	4	2		
χ^2_{total}/ndf	4.8	4.2	4.2	4.7	4.2	3.7
$\chi^2/ndp _{x_F}^{\pi^-}$	4.6	4.5	4.5	5.2	4.5	3.9
$\chi^2/ndp _{x_F}^p$	3.9	1.9	1.9	1.8	1.9	2.0
$\chi^2/ndp _{\sqrt{s}}^{\pi^-}$	9.7	4.4	2.5	9.3	4.4	2.1
$\chi^2/ndp _{\sqrt{s}}^p$	11.0	6.9	9.5	6.2	6.9	9.7
$\langle \mathcal{O}_8^{J/\psi} [^3S_1] \rangle$	3.6E-02	8.5E-02	1.6E-01	5.1E-02	8.5E-02	1.3E-01
	$\pm 9.9E-04$	$\pm 4.1E-03$	$\pm 4.7E-03$	$\pm 1.0E-03$	$\pm 4.1E-03$	$\pm 6.0E-03$
$\Delta_8^{J/\psi}$	1.7E-02	3.9E-02	8.3E-02	9.6E-03	3.9E-02	9.4E-02
$//'$	$\pm 9.5E-04$	$\pm 3.4E-03$	$\pm 4.1E-03$	$\pm 6.3E-04$	$\pm 3.4E-03$	$\pm 5.2E-03$
$\langle \mathcal{O}_8^{\psi(2S)} [^3S_1] \rangle$	9.3E-03	1.9E-02	3.4E-02	1.2E-02	1.9E-02	2.9E-02
	$\pm 3.6E-04$	$\pm 1.2E-03$	$\pm 1.4E-03$	$\pm 4.5E-04$	$\pm 1.2E-03$	$\pm 1.6E-03$
$\Delta_8^{\psi(2S)}$	9.1E-04	4.0E-03	8.7E-03	6.2E-04	4.0E-03	1.0E-02
	$\pm 1.8E-04$	$\pm 6.4E-04$	$\pm 7.0E-04$	$\pm 1.5E-04$	$\pm 6.4E-04$	$\pm 9.5E-04$

TABLE VIII. The reduced χ^2/ndf of values for the whole data sets and the χ^2 divided by the number of data point (ndf) for the pion-induced and proton-induced datasets with the systematic variation of charm quark mass m_c of 1.4, 1.5 and 1.6 GeV/ c^2 , and $\mu = \mu_R = \mu_F$ at 1.0, 2.0, and 4.0 m_c in NRQCD calculations and the corresponding input or best-fit LDMEs for xFitter pion PDFs. All LDMEs are in units of GeV³.

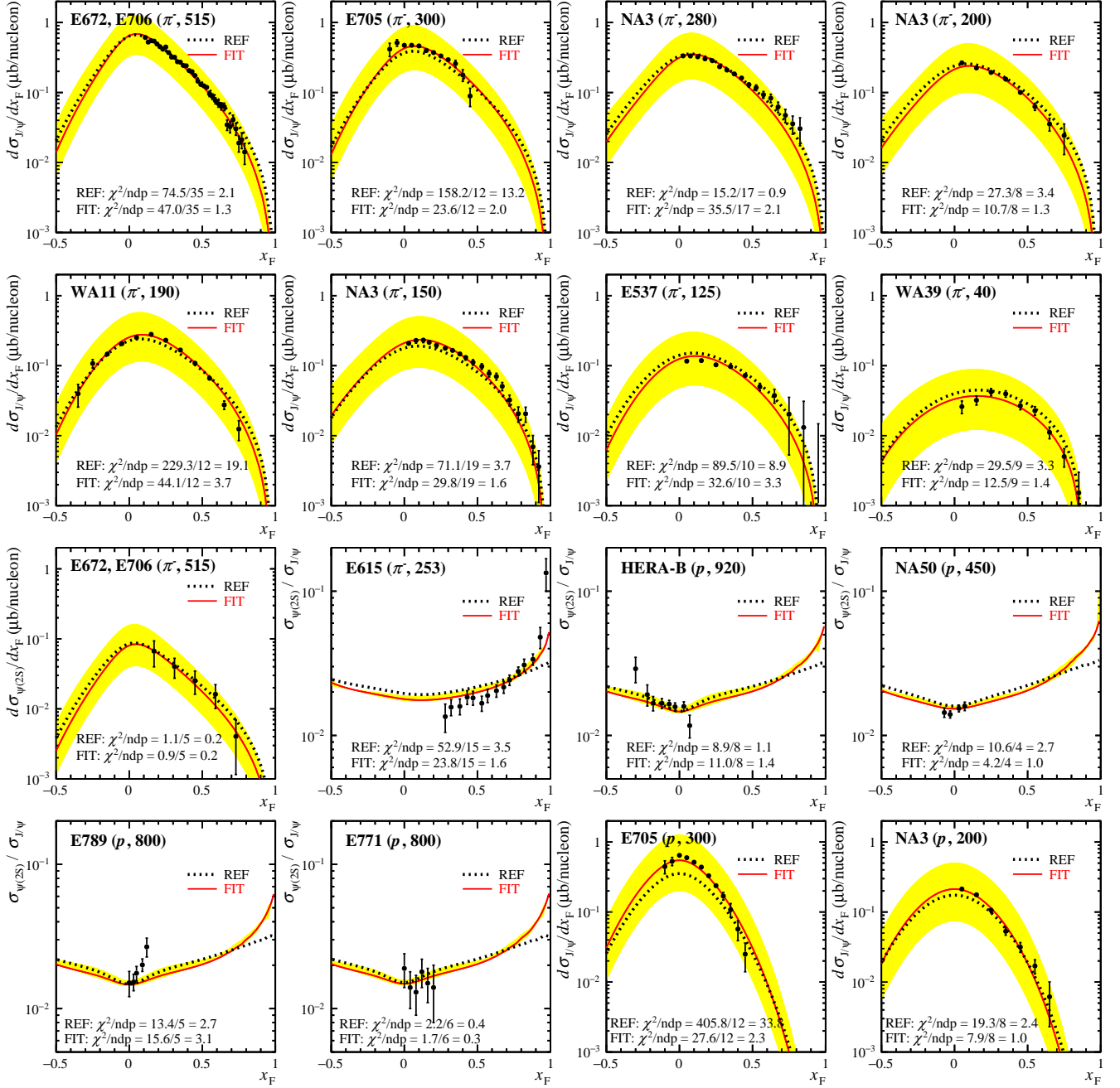


FIG. 22. Same as Fig. 2 in the main text while the yellow bands represent the cross section uncertainties corresponding to the scale and charm quark mass systematic variations, with the fixed LDMEs from "Fit" in Table III.

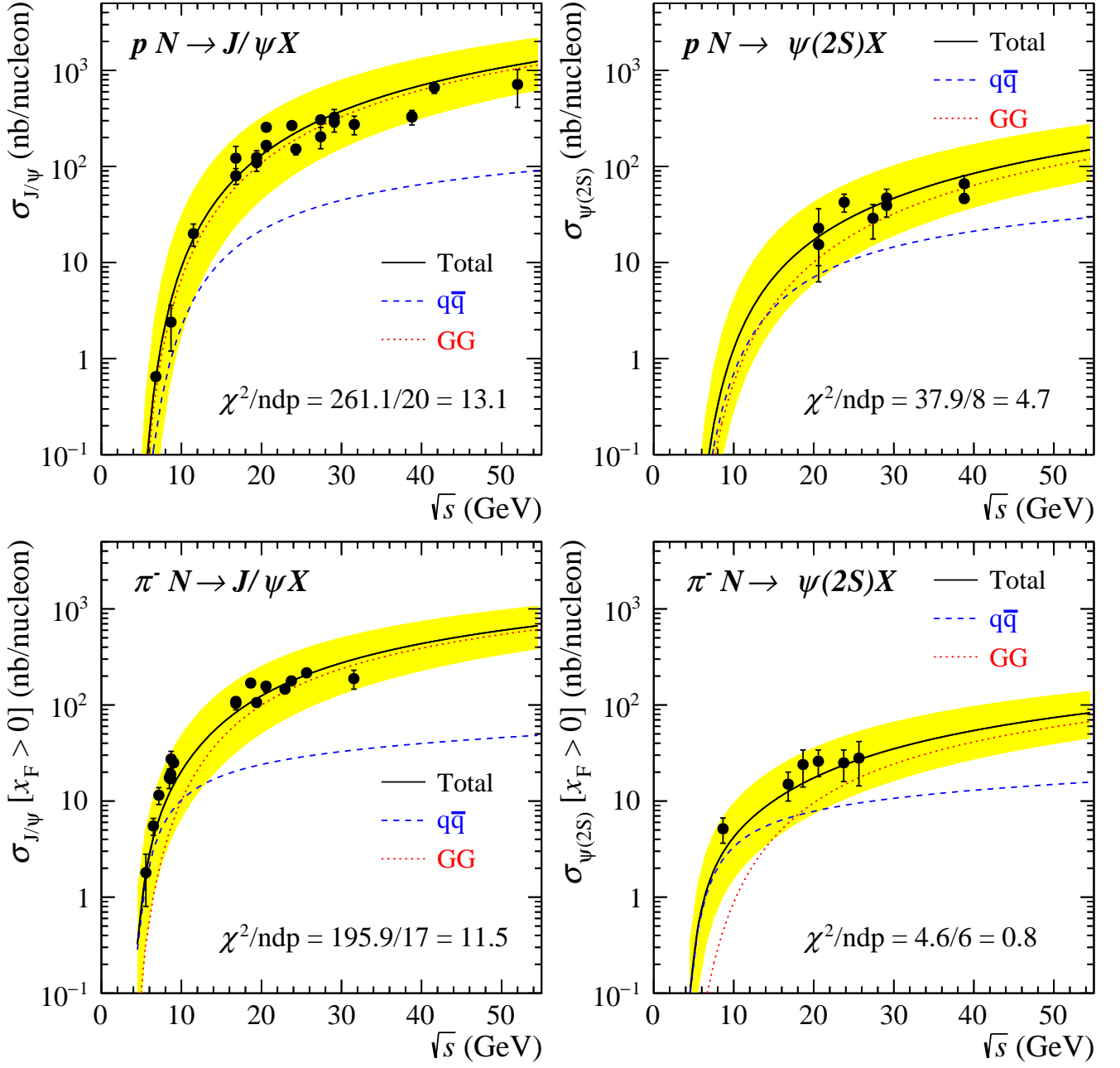


FIG. 23. Same as Fig. 8 in the main text while the yellow bands represent the cross section uncertainties corresponding to the scale and charm quark mass systematic variations, with the fixed LDMEs from "Fit" in Table III.